

## Abstract

Thermotropic liquid crystals exhibit phase transitions to unusual phases, also known as mesophases, that are neither liquids nor crystals; that is to say they are a confluence of fluidity and long-range order. The mesophases formed by the bent-core variety of liquid crystals have an extensive list of potential morphologies. For example, for some bent-core molecules that form the B4 phase, helical nanofilaments form. These chiral structures arise despite the fact that molecules are often achiral. Small alterations in structure can also have large implications for the handedness and degree of hierarchical self-assembly; as well as bringing about other changes e.g. blue structural colour. These twisted filaments can form further structures by splitting and braiding as well as forming coaxial heliconical layers. The complex morphologies of these liquid crystals exhibit complexity rivalling that of filaments in biological systems. Further analysis, however, is needed to elucidate general rules for the morphology and phase behaviour of these bent-core liquid crystals.

Simulations of atomistic and coarse-grained models are used in this project to provide insight into the complex phase behaviour of a group of bent-core molecules. Atomistic simulations have provided detail about the conformations of three bent-core mesogens in both the bulk and gas phase, elucidated properties of a phase change as well as displayed evidence of small nematic clusters forming in the isotropic phase. A coarse-grained model was also prepared to further study these systems.

# Contents

<b>1</b>	<b>Introduction and Literature Review</b>	<b>1</b>
1.1	Background . . . . .	1
1.2	Liquid Crystals . . . . .	1
1.3	Nematic Liquid Crystals . . . . .	4
1.4	Smectic Liquid Crystals . . . . .	5
1.5	Helical Nanofilaments . . . . .	6
1.6	Blue Phases . . . . .	7
1.7	Biological Applications of Liquid Crystals . . . . .	8
1.8	Bent-core Liquid Crystals . . . . .	9
1.9	Atomistic Simulations . . . . .	12
1.10	Quantum Molecular Dynamics Simulations . . . . .	13
1.11	Coarse-Grained Simulations . . . . .	14
1.12	Project . . . . .	15
<b>2</b>	<b>Computational Methods</b>	<b>16</b>
2.1	Atomistic Simulation . . . . .	16
2.1.1	Molecular Dynamics . . . . .	16
2.1.2	Stochastic Dynamics . . . . .	17
2.1.3	Mean Squared Displacement . . . . .	17
2.1.4	Order Parameter . . . . .	18
2.1.5	Pair Distribution Function . . . . .	18
2.2	Coarse-Graining . . . . .	18
2.2.1	Mapping . . . . .	19
2.2.2	Boltzmann Inversion . . . . .	19
2.2.3	Iterative Boltzmann Inversion . . . . .	20
2.3	Atomistic Model . . . . .	21
<b>3</b>	<b>Results and Discussion</b>	<b>22</b>

3.1	Atomistic Simulations . . . . .	22
3.1.1	Force Field Optimisation . . . . .	22
3.1.2	Stochastic Dynamics Gas Phase Simulations . . . . .	25
3.2	Atomistic Bulk Phase Simulations . . . . .	28
3.2.1	Core-Angle Dihedral Distributions . . . . .	30
3.2.2	Meta-Side Core-Tail Dihedral Distributions . . . . .	33
3.2.3	Para Core-Tail Dihedral Distributions . . . . .	35
3.2.4	Comparison of Meta and Para Core-tail Distributions. . . . .	37
3.2.5	Density . . . . .	38
3.2.6	Mean Squared Displacement . . . . .	39
3.2.7	Order Parameter . . . . .	42
3.2.8	$g_2(r)$ . . . . .	43
3.3	Coarse-Grained Simulations . . . . .	45
<b>4</b>	<b>Conclusion</b>	<b>48</b>
4.0.1	Atomistic Simulations . . . . .	49
4.0.2	Coarse-grained Simulations . . . . .	50
4.1	Future Work . . . . .	50
<b>References</b>		<b>52</b>
<b>Seminar Summaries</b>		<b>56</b>

## Acknowledgements

Thanks to Gary for his support and advice throughout the year (and his FORTRAN code), as well as to Prof. Mark R. Wilson for his time and comments. Tom is also not to be forgotten, his contributions have been a great help too, even if they were marred by his violent temper. I'd also like to thank Martin for his tips & tricks, as well as his 'jokes'. Thank you to Andrew for saying bye to Hoon for me.

# 1 Introduction and Literature Review

## 1.1 Background

Carrots have many uses, the most interesting of which, ought to be the propensity for generating entire fields of study based around mesogenic phases of matter.<sup>1</sup> Liquid crystals, as Otto Lehmann called them, were first observed by Friedrich Reinitzer in 1888.<sup>2</sup> Reinitzer, while investigating the melting points of various cholesterol derivatives, curiously noticed more than one ‘melting point’ of a supposedly pure substance. There was a first melting point at 145 °C into a cloudy liquid followed subsequently by one at 180 °C, turning it clear. Lacking a paradigm with which he could use as a backdrop to understand and contextualise what he had observed, an explanation eluded him. His observations were relegated to the epistemological purgatory of ‘mere facts’ and their importance and possible applications were not realised for years. Even though it has taken some time to reach this point, in modern times, liquid crystals have become ubiquitous. They appear in practically all modern day screens, as well as polymers, switchable windows, thermometers and a variety of other opto-electronic devices.<sup>3, 4, 5</sup>

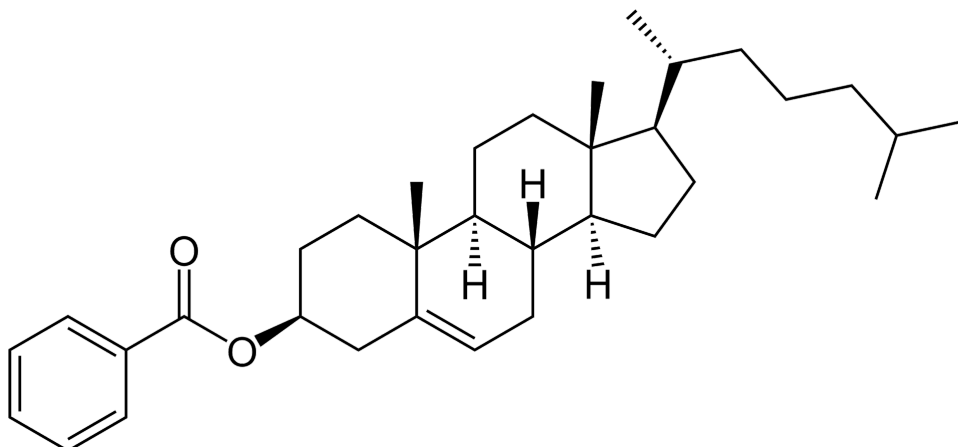


Figure 1: Cholesteryl benzoate, the liquid crystal that Reinitzer originally studied. The term ‘cholesteric phase’ is derived from the chiral mesophase that it forms.

## 1.2 Liquid Crystals

Liquid crystals (LCs) are phases of matter that contain at least one dimension of long range order. They are also known as mesophases; a confluence of the properties of both liquids and solids. Liquid crystals are not all identical, however, and can arise from multiple types of mesogen. From discotic (disk shaped) to calamitic (rod shaped), and can even have bent molecular cores.

Not only are there different varieties of mesogen but also different ways of ordering them. These mesophases exhibit unique physical characteristics e.g. nematic (from the Greek "νήμα" (nema), which means thread) which is only ordered in the sense of the direction that the calamitic liquid crystals are on average pointing (the director); or smectic (from the Latin "smecticus", meaning cleaning) that in addition to a director, is organised into layers orthogonal to the director. These layers also have an additional degree of freedom in their phase behaviour that the layers are not restricted to being orthogonal to the director and can be any angle between 0° and 180° relative to it. Nematic phases are the least ordered and most common phase, due to the fact they only have one dimension of long range order. Generally liquid crystals are found in either a smectic or nematic phase.

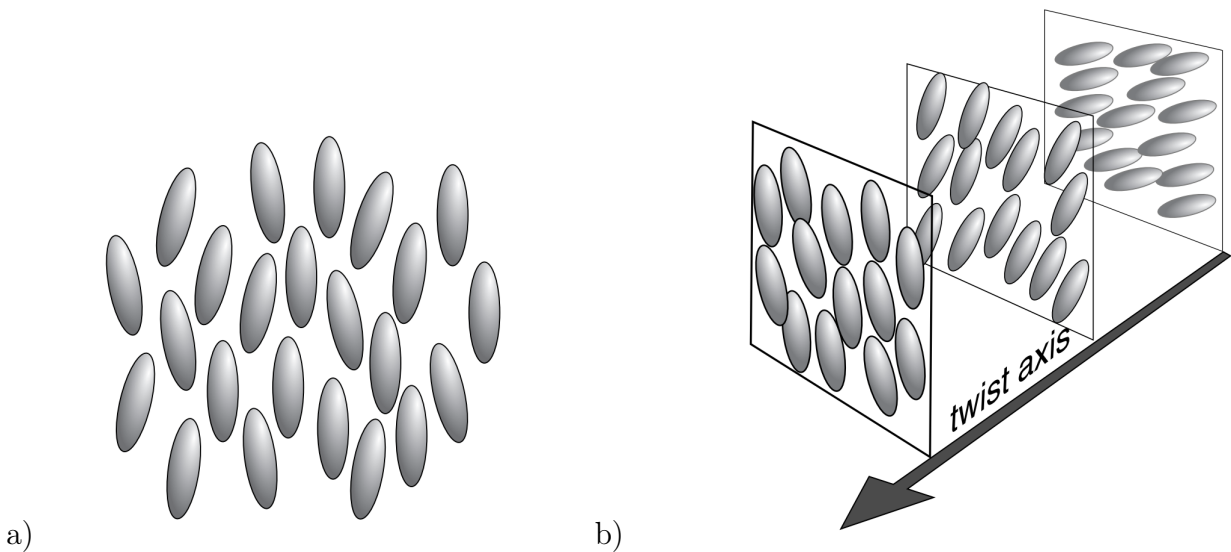


Figure 2: Examples of the two key liquid crystal phases related to the project: a) Nematic phase, b) Chiral Nematic phase.

The classification of LCs is also stratified with two more broad categories: one where the phase a LC takes can be altered by the temperature (thermotropic) and another where in addition to temperature, the LCs exist in solvent and as such concentration and pressure play a role (lyotropic). A basic requirement for a thermotropic mesogen is that it must be sufficiently rigid to maintain a degree of anisotropy in order to form nematic/smectic phases, these are intermediate phases (mesophases) which become crystalline at lower temperatures and isotropic at higher temperatures. Lyotropic mesogens are usually amphiphilic molecules, and in contrast to thermotropic mesogens they have an additional degree of freedom, their concentration. This allows them to form a myriad of structures at the same temperature, the structures they form being anything from micelles to lamellar phases

(lipid bilayers). The unique characteristics of each of the phases have given rise to applications, chiral nematic LCs, for example can be used as thermometers. LCD screens are applications of nematic LCs which are optically anisotropic and hence exhibit birefringence. Birefringence is when the refractive index has a different value when parallel to when its perpendicular to the director. Since the component along the director has a larger refractive index, this causes the interaction of plane polarized light to be dependent on what angle the plane of polarisation is to the director. When a bulk sample is viewed between cross-polarizers, distinctive bright and dark areas are observed. This effect coupled with an applied voltage to remove birefringence (via a Frederiks transition) allows the creation of basic LCD screens. Last but not least, discotic LCs are too used in opto-electronic devices for their ability to self assemble over long ranges, as well as their self healing properties.<sup>6</sup>

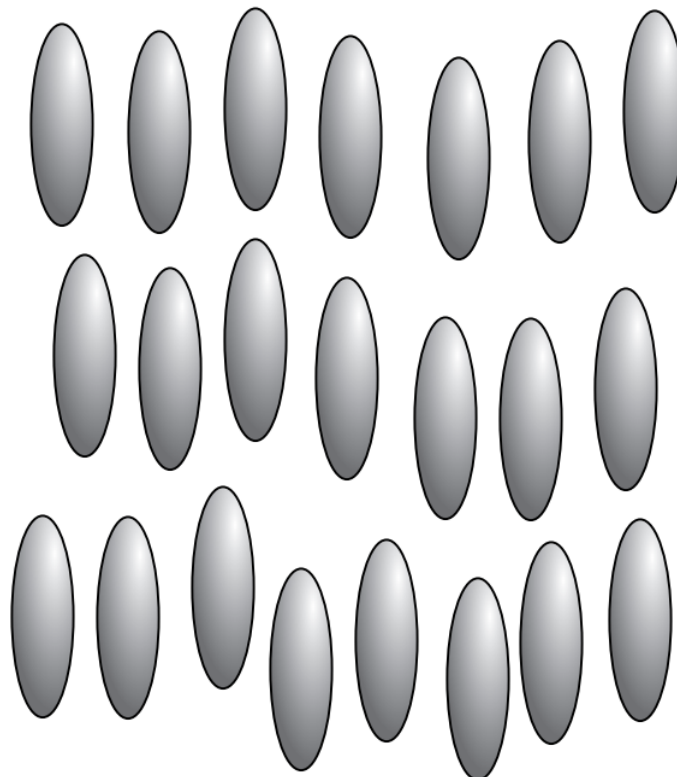


Figure 3: The Smectic A phase, which is comprised of layers which are perpendicular to the director.

### 1.3 Nematic Liquid Crystals

The proto-typical liquid crystal is the nematic liquid crystal, and the first type of liquid crystal discovered from the study of cholesterol. It is composed of a rigid, rod like (anisotropic) mesogen that can also have chiral properties. Nematics often have aromatic groups, since liquid crystallinity is more likely to occur if molecules have flat segments.<sup>7</sup> The organisation of nematic liquid crystals can be characterised by the director and tilt angle, the director is defined as a unit vector which is the average direction of all molecules, defined with respect to their long axis, and the tilt angle is the angle between any molecule and the director. The chiral properties of nematic liquid crystals are of particular interest, this phase, sometimes called “cholesteric” is a nematic phase where the helical director’s (which is perpendicular to the long director) orientation varies in direction throughout the medium periodically. The periodicity of this variation in the director is actually only half the distance of the twist, since the  $+/-$  sign of the director is irrelevant. These chiral twists have implications for the optical properties of a chiral nematic, since the pitch is usually on the same order of magnitude as the wavelength of visible light. Here, they can exhibit Bragg diffraction, which selectively diffracts wavelengths of light that are similar to helical pitch, exploited in liquid crystal thermometers.<sup>8</sup> The helical pitch is extremely sensitive. This is evidenced by the fact that the Bragg diffraction occurs only within a narrow temperature range, usually a few Kelvin, so ideal to see subtle changes away from body temperature. The other property of chiral nematic liquid crystals is their handedness, and this allows them to be used as circular polarisers, since polarized light that shares the same handedness as the helix will be selectively reflected.<sup>9</sup> Pitch is inversely dependent on temperature, with chiral nematic liquid crystals transitioning to become isotropic at higher temperatures. This is due to increased anharmonicity in thermal vibrations destroying the chiral structure.<sup>10</sup> Small structural changes in mesogens have surprisingly large consequences for their mesomorphic properties. For example, inversion of a single ester group in a LC chain can change the nematic-isotropic liquid transition temperature by 20 K.<sup>11</sup>

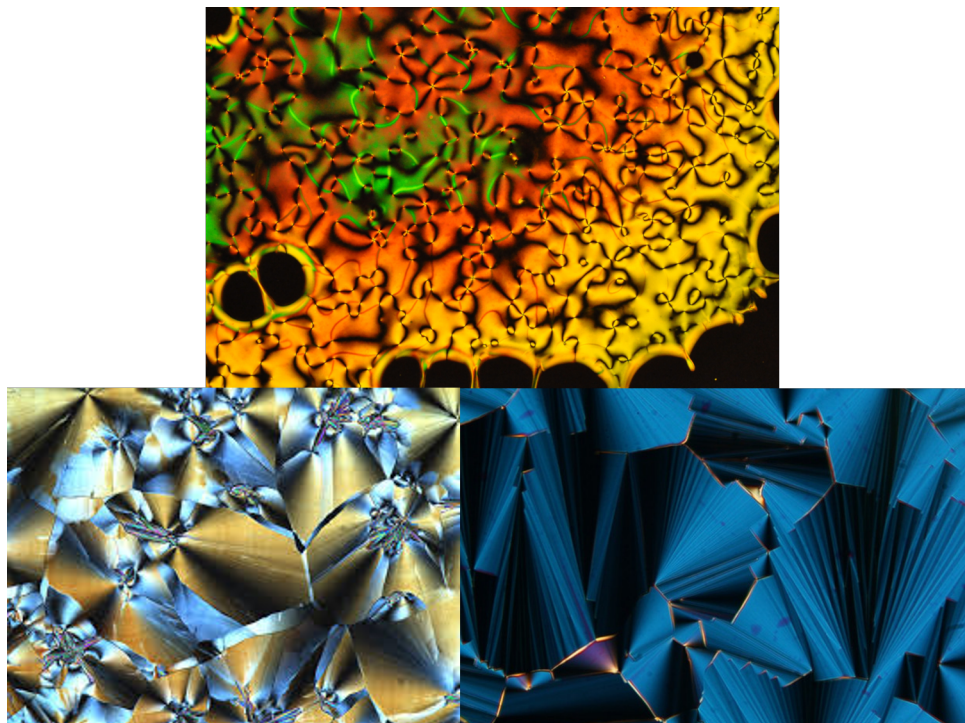


Figure 4: Liquid crystal phases as seen under a polarizing optical microscope. (Credit : Liquid Crystal Institute, Kent State University)

## 1.4 Smectic Liquid Crystals

Smectic liquid crystals are formed of layers of molecules which can move relative to each other, when the mesogens are normal to the layer plane then it is termed a smectic A phase (SmA), if they are tilted relative to the layer plane then it is said to be a smectic C phase (SmC). There are a variety of smectic phases, even hexatic smectic phases which have local hexagonal symmetry. Arrangement of mesogens in the smectic layers is determined by both intermolecular forces and molecular geometry. The types of forces that are important are, for example:  $\pi-\pi$  interactions, dipole-dipole interactions, as well as van der Waals forces to name a few.<sup>12</sup> Periodic structures can form in the layers, the most common being Focal Conic Domains (FCDs),<sup>13</sup> which are effectively a singularity in the director (since the energy of the singularity varies as a function of area it aims to minimise the focal surface and forms a hyperbolic sort of geometry). These defects have been suggested as a tool to synthesise nanoparticle clusters (fluorinated silica nanoparticles), by sintering. The sublimation of the LC material leaves spherical aggregates in orderly arrays.<sup>14</sup> This process has other applications too, the same sintering process can also be used to create superhydrophobic surfaces. Smectic LCs were placed on micro-pillar structures above the isotropic temperature, and cooled to produce toroidal FCDs. This dual scale roughness mimics lotus leaves and is an example of a micro-nano hybrid

structure. Chiral mesogens in SmC phases can cause spontaneous electric polarisation and gives rise to ferroelectricity, in which the spontaneous electric polarisation varies with tilt direction and has a periodicity the same as the pitch of the chiral SmC phase. If the mesogen was achiral, then due to symmetry the polarisation would average out, and there would be no overall effect. Applying a large DC electric field however, will cause alignment with the field and this effect is exploited in some display technologies.<sup>14</sup>

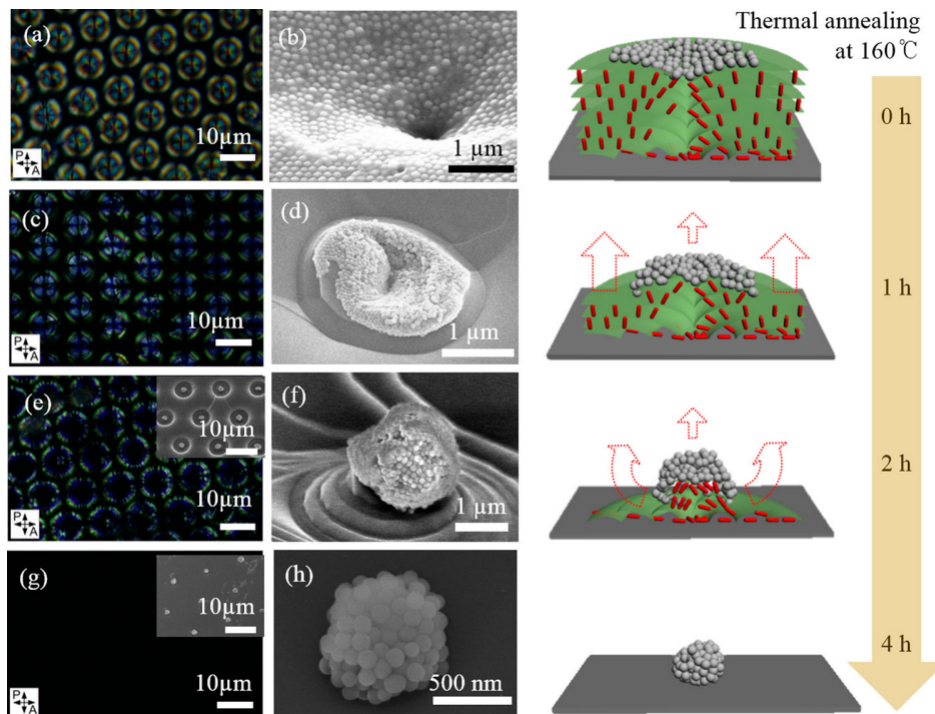


Figure 5: Coated focal conic domains can create a hydrophobic layer on a surface by exploiting their occurrence in the SmA phase of a liquid crystal, and upon being thermally sintered at 160 °C the liquid crystal sublimes, producing a nanoparticle of F-SiO<sub>2</sub>.<sup>13</sup>

## 1.5 Helical Nanofilaments

Self directed assembly of liquid crystals can also generate helical nanofilament (B4) phases which are neither crystalline nor conventional liquid crystals,<sup>15</sup> and one of the few known structures to preserve its nanoscale LC structure in a room temperature, semi-crystalline state.<sup>16</sup> These phases are generally formed when the isotropic phase of a bent-core liquid crystal is cooled slowly. In a helical nanofilament (HNF), smectic layers are stacked, and distorted slightly due to mismatch between layers causing a twisting arrangement in which a saddle-splay like configuration is adopted to relax any steric interaction originating from the intra-layer mismatch. These

twisted layers are what forms the helical nanofilaments. Heliconical coaxial layers can be parallel packed, braided or even be in 3D nest like structure. Generation of these helical nanofilaments is very sensitive to initial geometry of the mesogen, for example, whether a methyl group is added to the meta or para side determines whether helical microfilaments (HuFs) or Heliconical-layered nanocylinders (HLNCs) are formed, respectively.<sup>15</sup> These complex morphologies are usually investigated via X-ray diffraction, both scanning and transmission electron microscopy and atomic force microscopy. Dopants can be introduced into HLNCs to make nanoporous networks with the same structure but opposite handedness, and host a chiral liquid crystal guest. It has also been found that helical assembly can be made more efficient with the addition of gold nanoparticles, which become coated in bent-core LCs guiding formation of nanofibres.<sup>17</sup>

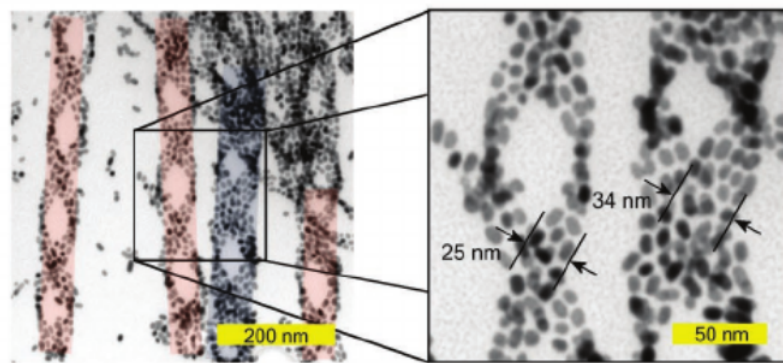


Figure 6: Gold nanoparticles, coated in bent-core mesogens promoting nanofilament growth.<sup>17</sup>

## 1.6 Blue Phases

Blue phases are highly ordered and exist in a narrow range of temperatures (0.5 - 1 K).<sup>18</sup> Discovered originally during the first observations of liquid crystals in 1888, and named due to the blue colour seen when observed with a polarising optical microscope. These are sensitive structures, but the temperature range that blue phases can exist over can be increased with a variety of techniques: one example is dispersing nanoparticles (or polymers), which end up trapped in the disclination lines of the phase and thus stabilise the phase. This has been shown to expand the temperature range by up to 5 K. The structure of blue phases can be understood in terms of chiral nematic phases, consisting of a double-twist structure, a twist of twists. Twisted columns of nematic LCs are twisted about a central point and over their helical axis, resulting in a frustrated structure, but more energetically favourable than a single twist (as in chiral nematics). These double twists are also

oriented in different directions with respect to each other and this orientation gives rise to three flavours of blue phases with differing symmetry. Phases I & II have cubic symmetry and phase III is an isotropic phase. The cubic symmetry is in reference to the disclinations of the blue phases, where the double twists meet and cause defects. Blue phase I being body centred cubic and II being face centered. Blue phases are of particular interest due to their application in fast response displays and lasing.<sup>19, 20</sup>

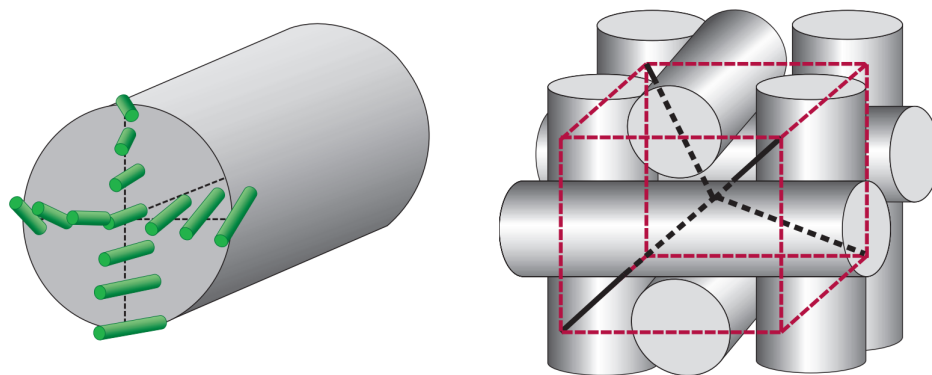


Figure 7: Example of a blue phase of liquid crystals.<sup>21</sup>

## 1.7 Biological Applications of Liquid Crystals

Liquid crystals hold the key to the complexity of life, their supramolecular and self-assembly character being an integral feature at all length scales. Glycolipid cell membranes are a prime example of a biological liquid crystal.<sup>22</sup> LCs have an array of applications in biological/medicinal chemistry, from drug delivery<sup>23</sup> to being used as a substrate for stem cell cultures.<sup>24</sup> In fact, LCs can be used to detect cancer by using specific biomarkers that can be detected if an LC with a large birefringence is chosen, because the interaction between antibodies and biomarkers disrupts the optical texture of the LC. This technique affords immunodetection for concentrations of 0.01 to 0.1 µg / ml, much more sensitive than the standard fluorescence immunoassay which has a threshold of merely 4 to 5 µg / ml.<sup>25</sup>

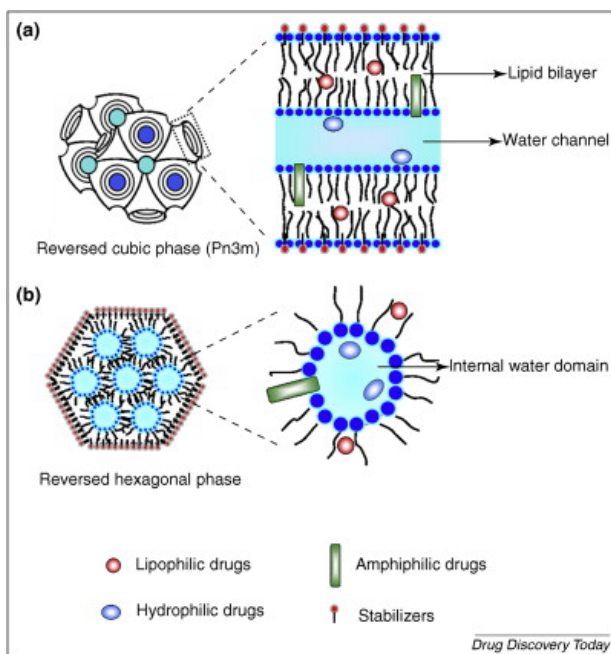


Figure 8: Potential drug delivery system using the high interfacial area and compartmentalisation of cubic mesophases of liquid crystals to administer hydrophilic, amphiphilic or lipophilic drugs.<sup>23</sup>

## 1.8 Bent-core Liquid Crystals

Liquid crystals can have further interesting properties, especially when the mesogen takes an unusual shape. For example, a particular bent-core variety of liquid crystal was discovered by Japanese scientists (actually they merely revived earlier work, as bent-core liquid crystals were known to Daniel Vorländer in 1929), the discovery was the synthesis of the prototypical molecule (*s*, 1,3-phenylene bis[4-(4-n-octyloxyphenyliminomethyl)] benzoate; P-*n*-O-PIMB) and ushered in a new era in liquid crystal research. Non-rod-like molecules were originally thought to be unsuitable for forming liquid crystal phases owing to the fact they can rotate around their molecular axis, creating a large excluded volume and violating any liquid crystalline type behaviour.<sup>26</sup> These bent-core mesogens were found to form domains of chiral superstructures despite the mesogen itself being achiral, the first true fluid system to show spontaneous chiral symmetry breaking in bulk.<sup>27</sup> There are eight such phases B1-B8,<sup>28</sup> the B1 phase is columnar whilst the most studied phase is the B2 phase due to its ferroelectric-like properties. This is caused by a dipole in the bent-core creating a spontaneous polarization in the smectic layer. The superstructure of bent-core liquid crystals can be influenced by substituents, for example fluorine can alter the mesophases formed when an electric field is applied due to its electronegativity. This effect is modulated by chain length, although substituents in

the centre of the bent-core mesogen seem to have little effect.<sup>29</sup> Interestingly, doping chiral liquid crystals with achiral bent-core mesogens has been found to increase the chirality of the system, rather than diluting the effect as would be expected.<sup>30</sup>

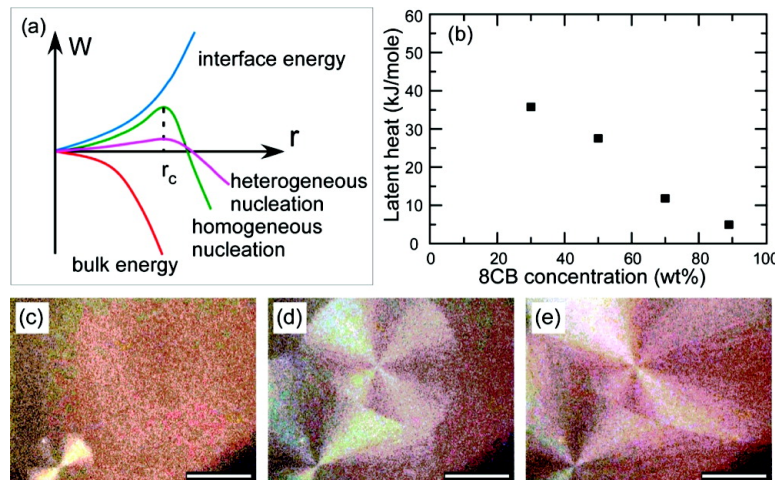


Figure 9: Energetics and real-time observation of chiral domain nucleation and growth of the achiral bent-core dopant NOBOW B4 phase in 8CB/NOBOW mixtures. (a) Competition between the energy gained by creating a new volume of B4 (red curve) and the cost of surface tension (blue curve) results in a finite energy barrier to homogeneous nucleation (green curve) and a critical radius  $r_c$ . For heterogeneous nucleation, such as in the case of chiral doping,  $r_c$  is the same as for homogeneous nucleation, but the energy barrier of domains with the same chirality as the dopant is reduced (magenta curve). Figure and caption reproduced.<sup>31</sup>

This slightly counter-intuitive result is explained by the fact that achiral molecules can have two axially chiral conformers, which when they occur allow the achiral mesogen to behave as if it were chiral. Bent-core liquid crystals can also generate superior phases to what is possible with simple calamitic mesogens. For example, bent-core blue phases are more stable across a wider range of temperatures.<sup>32</sup>

Bent-core liquid crystals also show promise for optical storage devices, with photosensitive azo-containing mesogens undergoing photoconversion from a nematic phase composed of trans stereoisomers to the metastable isotropic phase of cis stereoisomers. When these mesogens are illuminated with UV light at a wavelength of roughly 365 nm, it triggers a  $\pi \rightarrow \pi^*$  transition, which causes a conformational change.<sup>33</sup>

This transition causes the bent-cores to become W shaped, and creates a new isotropic phase due to the inability of the mesogens to nicely pack, caused by the steric hindrance of their new geometry. The cis-trans isomerism can take place within minutes, but the trans-cis relaxation can take 4 – 16 hours. Fine tuning substituents to increase the thermal relaxation time could lead to novel optical storage devices.

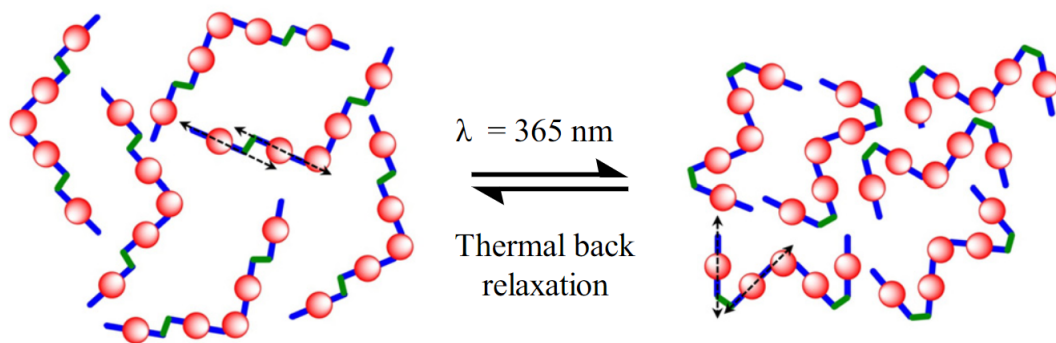


Figure 10: Schematic representation of the photoisomerisation of diazo bent-cores. The cis isomers of diazo bent-core mesogens at room temperature are irradiated with UV light at 365 nm, causing the thermodynamically stable trans configuration (nematic phase) to convert into the meta-stable cis configuration (isotropic phase).<sup>33</sup>



Figure 11: Prototype optical storage device, observed under crossed polarisers.<sup>33</sup>

The reflective regions of the device are the cis-nematic phase, which hasn't been irradiated with UV light whilst the dark regions corresponds to the irradiated trans-isotropic phase.

## 1.9 Atomistic Simulations

An important method for advancing our understanding is simulation, sometimes seen as the third type of science, along with experimental and theoretical studies. Simulation allows intimate examination of the properties of materials that are hard to study experimentally. Molecular simulations can be fine grained simulations, or coarse-grained. Fine grained simulations are more computationally costly for the bulk compared to coarser methods, so although accurate, they can be infeasible to use in practice and often coarse-graining techniques are tactically deployed. Sacrifices must be made on the altar of computational power, for example a simple way for modelling a non-bonded potential is by using a Lennard-Jones potential,<sup>34</sup> which is a computationally inexpensive yet less accurate choice. Simulations generally solve Newton's equations numerically (a justified approximation because nuclei are heavy enough to be considered classical), taking positions and velocities to calculate forces and therefore accelerations and then updating positions in an iterative manner to simulate complicated systems. This is done with a computer algorithm (for example the Verlet velocity algorithm)<sup>35</sup> which is designed to require little memory, be simple, allow large time-steps and dutifully follow classical trajectories. Atomistic simulations can allow calculation of important properties, such as radial distribution functions or bulk diffusion coefficients, but longer scale phenomenon are harder to study with atomistic simulations since the size of the time step is determined by the fastest process. This is usually on the order of femtoseconds, requiring inordinate CPU time to simulate, say, phenomenon on the millisecond timescale. Even though atomistic simulations can be computationally expensive, systems with hundreds of thousands of atoms are regularly run. An active area of development is the refinement of force fields, which are used as approximations to intractably complicated quantum mechanical calculations.<sup>36</sup> These approximations can make simulations of systems where quantum effects are dominant (for example a protein containing a transition metal) difficult, but this can be potentially overcome by adopting a hybrid method that incorporates quantum calculations to classical approximations. Another common approximation is the assignment of partial charges before the simulation is run, but in reality the charge distribution in a molecule is dynamic and dependent on what sort of environment it is in so again, this is at the expense of accuracy. Molecular docking is a common practical application for atomistic MD simulations, where a small molecule is simulated in a number of poses within a “binding region” to identify potential binding sites. A score can then be calculated which takes into consideration sterics and physicochemical interactions. This score can be used as a proxy for the binding free energy and allow calculation of dissociation constants. Serendipitously, the calculations required to perform these types of

simulations are also the same ones computer games use for their graphics, and since GPU (Graphics Processing Unit) design is a multi-billion pound industry, a lot of time and money has been invested in making them extremely powerful, meaning GPUs can speed up MD simulations by an order of magnitude or more.<sup>37</sup>

## 1.10 Quantum Molecular Dynamics Simulations

Classical molecular dynamics simulations rely on certain approximations, namely the decoupling of electronic and nuclear motion (Born-Oppenheimer approximation). Although classical molecular dynamics simulations are invaluable, they can fail to describe certain processes, such as excited states.<sup>38</sup> Excited states are important to understand as they are integral to many fields, from photochemistry to synthesis. The fundamental aim of *ab initio* quantum molecular mechanics is to solve the time dependent Schrödinger equation

$$i\hbar \frac{\partial}{\partial t} \Psi(\mathbf{r}, t) = \hat{H}\Psi(\mathbf{r}, t), \quad (1)$$

this method is more accurate and applicable to a wider range of chemical systems compared to classical molecular dynamics but is not without its problems. Even relatively simple low energy systems can have an impractical number of quantum states, since the numerical solution requires exponentially more computation with the number of particles.<sup>39</sup> This complexity creates a trade-off between the practicality of a computation, that is how much CPU time is required, and the accuracy. One approach to surmount this problem is to mix classical and quantum methods, a hybrid, that has the efficiency of the former whilst retaining the accuracy of the latter. For example, treating slow nuclear motion as classical but incorporating nonadiabatic transitions in the calculation for the forces of the motion.<sup>40</sup> This is of particular use in say, enzyme binding (due to conformational changes upon binding). In this case, there are peripheral atoms unrelated to binding that it suffices to treat classically, but atoms that are closer to the binding site require a quantum treatment. This method can reduce the nonadiabatic region to a localised area comprised of only tens of atoms, a vast improvement. Quantum force fields offer not only the advantage of accuracy but also one of transferability, with traditional forcefields usually generating partial charges with semi-empirical calculations. This leaves them vulnerable to not correctly generating other parameters, such as Van der Waals radii which depend on partial charges as well as environment.<sup>41</sup> Quantum force fields have recently been automatically generated by Cole *et al.* that address these issues, instead of using Mulliken partial charges that replace some integrals with parameters, like GAFF, partial charges can be generated by iteratively opti-

mising the average electron density around atoms and integrating over all space. With the only parametrisation of this method being the radii for each element. Using this technique 109 small organic molecules' forcefields were generated with the QUBEKit (QUantum mechanical BEspoke Kit) with competitive accuracy.<sup>42</sup>

## 1.11 Coarse-Grained Simulations

Mesogenic systems are some of the most complex in chemistry, their properties rely on an intricate interplay of factors across multiple orders of magnitude, from charge distribution to slight changes in molecular geometry. The most complex chemical systems, those relevant to life, are particularly hard to study using atomistic simulations as they are limited by algorithmic efficiency and processing power, due to the size of the systems involved. Protein folding for example, is a fiendish task and atomistic simulation can take an inordinate amount of CPU time. Coarse-grained models can allow these systems to be investigated on account of their increased simplicity and therefore, efficiency, at the expense of accuracy without having to rely on quantum techniques. This moves the problem to that of choosing a coarse-graining scheme that allows the keeping of the 'essential character' of the system whilst reducing the computational requirements. In general, there are three types of coarse graining, top down, bottom up and toy models. Top down models are based on thermodynamic parameters, and seek to reproduce experimental data by fitting potentials. An example of top-down parameterisation is SAFT<sup>43</sup> (Statistical Associating Fluid Theory) which aims to parametrise the Helmholtz free energy and using it to predict other macroscopic quantities like density, Gibbs free energies or heat capacities. There are multiple variants of SAFT fit for different situations (e.g. SAFT- $\gamma$  Mie which in essence is calculating potentials for hard spheres, linking them covalently to form chains, then adding dispersion forces and hydrogen bonding interactions in order to calculate the Helmholtz free energy). The second type of coarse-graining is bottom-up coarse graining, and is more 'physics based'. It involves grouping similar heavy atoms into 'beads' and assigning them a handful of different bead-types, with separate *ab initio* bonded potentials. Non-bonded potentials can be obtained via iterative Boltzmann inversion (IBI – see section 2.2.3) which takes the radial distribution function from an atomistic simulation trajectory and converts it into a potential. This method is particularly expensive since all potentials must be fitted simultaneously and affect one another, meaning that bottom-up coarse grained models scales with the number of bead types, and limiting its scope for very complex molecules. Thirdly, toy models are not very quantitative in relation to the real system, but aim to give qualitative physical insight into systems, whilst

being very computationally inexpensive. Coarse-graining faces two big challenges: representability and transferability. Representability is whether the system accurately predicts macroscopic quantities at the thermodynamic statepoint at which it is parametrised,<sup>44</sup> this is often absent when the coarse graining process removes essential properties; for example, a system where the dipole moment is important represented by a single bead (a point cannot have a dipole). Care also has to be taken with entropy in coarse-graining, since entropy is usually affected more than enthalpy by the coarse-graining procedure, and this affects the relative balance of the two and can cause diminished the accuracy of any model created.<sup>45</sup> Transferability concerns whether a model can be predictive when parameterisation data is not available, a useful property, since synthesis can be lengthy and costly; particularly of interest to pharmaceutical companies. They tend to avoid having to synthesise thousands of compounds systematically to test their efficacy, if they can. These problems apply to both top-down and bottom-up models and strike at the heart of what coarse-graining is about, they are questions of whether a model is transferable, or whether it correctly represents a system, and they are deep questions indeed.

## 1.12 Project

This project aims to understand the chiral self-assembly of tris-biphenyl diester bent-core liquid crystals (TBD-LCs) using atomistic and coarse grained models. The hierarchical structures (helical mesophases) they form are of extreme interest, and a better understanding of their mesogenic phases is needed. One way to elucidate their properties is with simulation.

The main objectives of this project are:

- To analyse conformations of TBD-LCs;
- To understand bulk behaviour of TBD-LCs;
- To see if pre-transitional behaviour occurs near the isotropic transition point;
- To interrogate phase transition behaviour;
- To create a coarse-grained model of TBD-LCs.

## 2 Computational Methods

### 2.1 Atomistic Simulation

Atomistic simulations were carried out using GROMACS 2016.5; a molecular dynamics package able to perform calculations as well as data analysis.<sup>46</sup> GROMACS was used in conjunction with the general AMBER force field (GAFF).<sup>47</sup> The Antechamber package from AmberTools18 was employed with the AM1-BCC method (which generates point charges) to automatically generate atom types and charges.<sup>48,49</sup> The ACPYPE script was used to convert the Antechamber output files into GROMACS format.<sup>50</sup> The potential functions which define the total potential energy of the system in a simulation are given by

$$\begin{aligned} E^{\text{tot}} = & \sum_{\text{bonds}} K_r(r - r_{\text{eq}})^2 + \sum_{\text{angles}} K_\theta(\theta - \theta_{\text{eq}})^2 \\ & + \sum_{\text{proper}} \sum_{n=0}^5 C_n (\cos(\psi))^n + \sum_{\text{improper}} k_d (1 + \cos(n_d \omega - \omega_d)) \\ & + \sum_{i>j}^N \left[ 4\epsilon_{ij} \left( \left( \frac{\sigma_{ij}}{r_{ij}} \right)^{12} - \left( \frac{\sigma_{ij}}{r_{ij}} \right)^6 \right) + \frac{1}{4\pi\varepsilon_0} \frac{q_i q_j}{r_{ij}} \right], \end{aligned} \quad (2)$$

where  $r_{\text{eq}}$  and  $\theta_{\text{eq}}$  are equilibrium bond lengths and angles respectively.  $K_r$ ,  $K_\theta$  and  $k_d$  are force constants associated with the bond, angle and improper dihedral terms respectively. Non-bonded interactions are described by a Lennard-Jones and Coulomb potential where  $\epsilon_{ij}$  and  $\sigma_{ij}$  are the standard Lennard-Jones parameters and where  $q_i$ ,  $q_j$  and  $\varepsilon_0$ , are the partial charges and permittivity constant respectively. For alkanes, the following proper dihedral potential is often used<sup>51</sup>

$$V_{rb}(\phi_{ijkl}) = \sum_{n=0}^5 C_n (\cos(\psi))^n,$$

This is the Ryckaert-Belleman function, where  $C_n$  are constants that can be changed to fit a particular *ab initio* potential.

#### 2.1.1 Molecular Dynamics

Force fields use potential energy functions to calculate the force,  $F_i$ , for any atom  $i$  in the system. Forces are defined as the negative first derivative of a potential energy function,  $V(\mathbf{r}_i)$ . For Molecular Dynamics simulations this takes the form

$$\mathbf{F}_i = -\frac{\partial E^{tot}}{\partial \mathbf{r}_i}. \quad (3)$$

Molecular dynamics simulations iteratively solve Newton's equations of motion which are

$$\mathbf{F}_i = m_i \frac{\partial^2 \mathbf{r}_i}{\partial t^2}; \quad \mathbf{v}_i = \frac{\partial \mathbf{r}_i}{\partial t}; \quad \mathbf{F}_i = m_i \frac{\partial \mathbf{v}_i}{\partial t} \quad , \text{ for } i = 1 \dots N \quad (4)$$

This iterative process is done by a leap-frog algorithm which uses the force  $\mathbf{F}_i(t)$  to update positions  $\mathbf{r}_i$  and velocities  $\mathbf{v}_i$  at time  $t$ , advanced according to a timestep  $t - \frac{1}{2}\Delta t$ , which is chosen to be as large as possible whilst retaining accuracy. This classically simulates the trajectory of molecules by the relations below

$$\mathbf{v}_i(t + \frac{1}{2}\Delta t) = \mathbf{v}_i(t - \frac{1}{2}\Delta t) + \frac{\Delta t}{m_i} \mathbf{F}_i(t), \quad (5)$$

$$\mathbf{r}_i(t + \Delta t) = \mathbf{r}_i(t) + \Delta t \mathbf{v}_i(t + \frac{1}{2}\Delta t). \quad (6)$$

A suitable time step,  $\Delta t$ , must be carefully selected so that the fastest motions in the system are captured yet still allow the simulation to run efficiently.

### 2.1.2 Stochastic Dynamics

Stochastic dynamics supplement molecular dynamics with random perturbations performed on all atoms as well as adding a friction term. The perturbation is chosen as to be large enough to move the structure away from the initial minimised conformation but not too large such that it causes the molecule to enter high-energy local minima, and to sample a proper Boltzmann distribution of energies.<sup>52</sup> These random perturbations and friction term are represented in Newton's equations as

$$m_i \frac{\partial^2 \mathbf{r}_i}{\partial t^2} = \mathbf{F}_i - m_i \gamma_i \frac{\partial \mathbf{r}_i}{\partial t} + \dot{\mathbf{r}}_i \quad (7)$$

where  $\gamma_i$  is the friction constant and  $\dot{\mathbf{r}}_i$  is a noise process which adds randomness to motion.

### 2.1.3 Mean Squared Displacement

Average properties like the diffusion coefficient, can be determined from molecular dynamics simulations, the three dimensional diffusion coefficient is given by

$$D = \frac{1}{3} \int_0^\infty \langle \mathbf{v}_i(t) \cdot \mathbf{v}_i(0) \rangle dt \quad (8)$$

Where  $\mathbf{v}_i(t)$  is the centre-of mass velocity of a single molecule.

At long times, the Diffusion coefficeint  $D_A$  of particles of type  $A$  can be determined via the Einstein relation (taking care to correct for molecules that have transported across a periodic boundary), which is

$$D = \lim_{t \rightarrow \infty} \frac{d}{dt} \frac{1}{6} \langle |r_i(t) - r_i(0)|^2 \rangle. \quad (9)$$

#### 2.1.4 Order Parameter

Liquid crystals can have both long range positional and orientational order, which it can be useful to quantify. Orientational order for example can be characterized by order parameter,  $S$ , (magnitude) and direction (director),  $\mathbf{n}$ . Once a long molecular axis has been defined, the order parameter can be given as

$$\hat{S}_2 = \langle P_2 \cos(\theta) \rangle = \langle \frac{3}{2} \cos^2 \theta - \frac{1}{2} \rangle, \quad (10)$$

where  $P_2$  is a second order Legendere polynomial.

#### 2.1.5 Pair Distribution Function

Distributions functions measure the average value of a property as a function of an independent variable.<sup>53</sup> Structural quantities can be obtained such as the pair distribution function  $g(r)$ , of a liquid crystal. This is the probability of finding a pair of particles as a function of distance, averaged over pairs and defined by

$$g(r) = \frac{V}{N^2} \langle \sum_i \sum_{j \neq i} \delta(r - r_{ij}) \rangle, \text{ where } r_{ij} = r_i - r_j, \quad (11)$$

where  $V$  is volume,  $N$  is the number of particles and  $r$  is position. A radial distribution has a value of 0 at extremely short distances, because molecules cannot be in the same place. An initial peak is usually followed by subsequent, smaller peaks which represent some sort of order e.g. for solvated ions there is usually an initial peak representing the primary solvation shell, followed by a smaller peaks representing secondary and tertiary etc. solvation shells. At long ranges the radial distribution function tends to a value of 1, which implies that the molecules are no longer influenced by each other and are uniformly distributed.

## 2.2 Coarse-Graining

Coarse-grained simulations were carried out using Versatile Object-oriented Toolkit for Coarse-graining Applications (VOTCA);<sup>54</sup> a coarse-graining program developed at the Max Planck Institute for Polymer Research. The coarse-graining toolkit

was used and bonded potentials obtained via Boltzmann inversion, and non-bonded potentials obtained via iterative Boltzmann-inversion (IBI). Initial geometry was created by using the centre of mass of heavy atoms and coarse graining at a resolution of 4:1 heavy atoms:bead. 9 types of bead were created initially. The scheme was simplified to 3 types however, to aid IBI convergence.

### 2.2.1 Mapping

Atomistic representations are related to a coarse-grained one by a mapping file, which is a topology of the coarse-grained molecule and a list of maps. Maps are a set of weights,  $c_{Ii}$  for an atom  $i$  belonging to bead  $I$ . Atoms are assigned to beads at some specified ratio, usually three to four heavy atoms per coarse-grained bead (Figure 10).

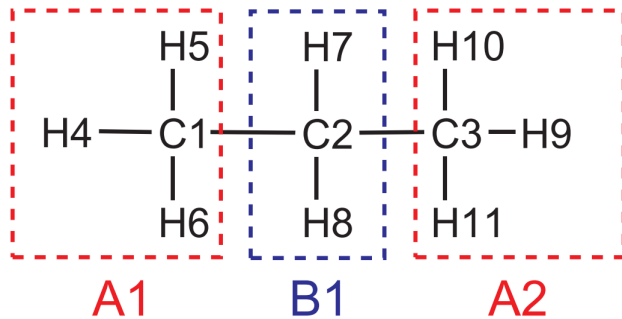


Figure 12: Atom labeling and mapping from an all-atom to a united atom representation for a propane molecule.

Beads can be stratified by type by assigning different properties depending on chemical environment. Bonded interactions are then assigned for angles, dihedrals and bonds for these beads via Boltzmann inversion.

### 2.2.2 Boltzmann Inversion

Bonded potentials,  $U(q)$ , were obtained from the equilibrated reference atomistic simulations by simple Boltzmann inversion, where independent degrees of freedom,  $q$ , obey the Boltzmann distribution

$$P(q) = Z^{-1} \exp [-\beta U(q)] \quad (12)$$

Where  $Z$  is the partition function, and  $\beta$  is thermodynamic temperature. Once  $P(q)$  is established then a coarse-grained potential can be generated by inverting the probability distribution  $P(q)$  of a variable  $q$  e.g. bond angle or bond length

using the relation

$$P(q) = -k_B T \ln P(q) \quad (13)$$

### 2.2.3 Iterative Boltzmann Inversion

Non-bonded potentials are generally generated by iterative Boltzmann inversion (IBI) methods, which aim to reproduce the radial distribution function of a reference system. IBI is a series of sequential Boltzmann inversions based on the previously generated potentials (the first step uses simple ‘guess’ potential),  $U$ , which are updated via the potential update  $\delta U$  and used in the next iteration, repeated until the radial distribution function has converged to within a specified tolerance. The iterative relations are

$$U^{(n+1)} = U^n + \lambda \Delta U^n, \quad (14)$$

$$\Delta U^n = k_B T \ln \frac{P^n}{P_{\text{ref}}} = U_{\text{PMF}}^{\text{ref}} - U_{\text{PMF}}^n, \quad (15)$$

where  $\lambda$  is a numerical factor which helps to stabilise the scheme.  $U_{\text{PMF}}^{\text{ref}}$  is the reference potential of mean force, and  $U_{\text{PMF}}^n$  is the potential mean force. The total number of interactions,  $N$ , needed to be fitted is given by

$$N = \frac{n(n+1)}{2} \quad (16)$$

where  $n$  is the number of beads.

### 2.3 Atomistic Model

An atomistic model was created using SCIGRESS,<sup>55</sup> a molecular modelling suite. An initial Energy minimisation was performed on each mesogen using the MM3 forcefield.

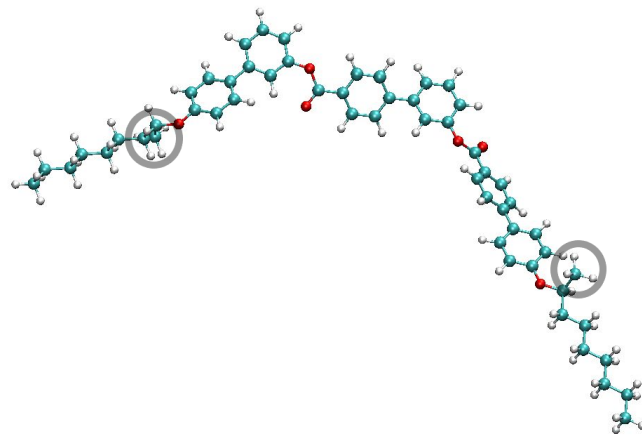


Figure 13: The doubly chiral centered mesogen, m,p-TBD, with chiral groups highlighted.

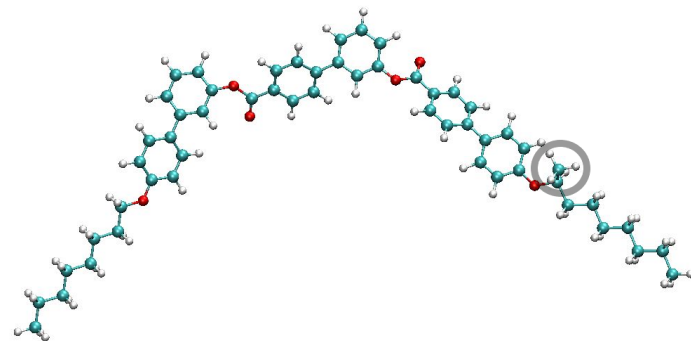


Figure 14: The singly chiral centered mesogen, m-TBD, with chiral groups highlighted.

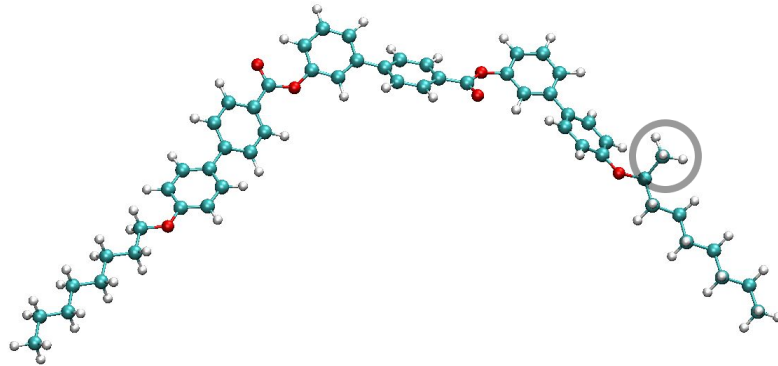


Figure 15: The singly chiral centered mesogen, p-TBD, with chiral groups highlighted.

### 3 Results and Discussion

#### 3.1 Atomistic Simulations

##### 3.1.1 Force Field Optimisation

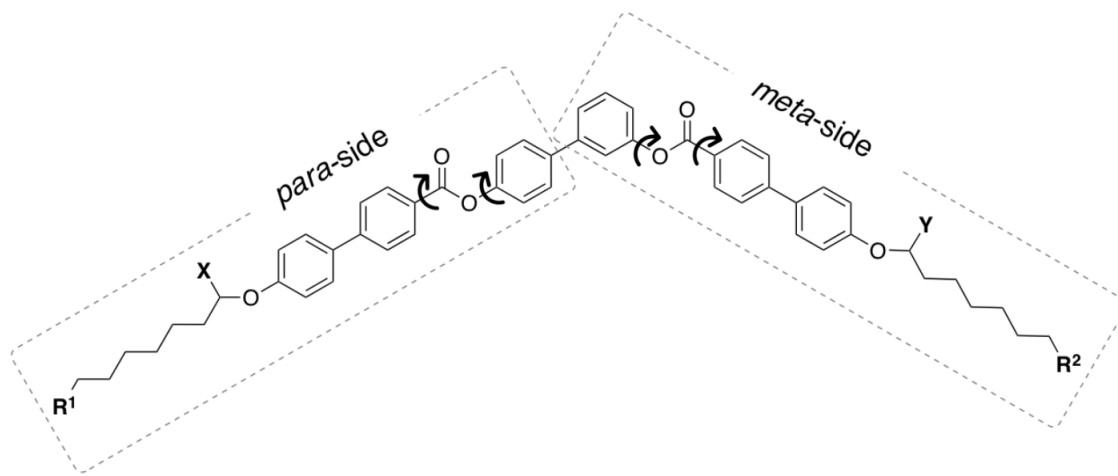


Figure 16: Schematic of a general tris-biphenyl diester bent-core mesogen, with modified GAFF-LCFF dihedrals highlighted. Groups X and Y in this project are configured to either be hydrogen, or are used to induce chirality via a methyl group.

Adding chiral groups to the general TBD-LC can have significant impact on their mesomorphic properties, altering not only what types of phases appear but also their

handedness - depending on the stereoisomer. There are three variants of the general (S)-TBD-LC that are examined in this project, two with a single chiral centre on each side (m-TBD on the meta side, and p-TBD on the para side) and one with two chiral centres (one on each side, m,p-TBD). The mesogens are shown in figures 13 – 15.

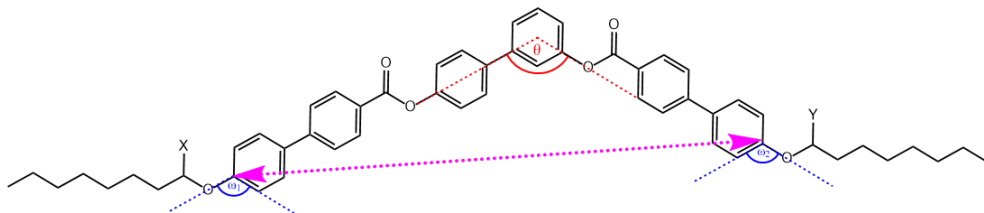


Figure 17: Core-angle,  $\theta$ , and core-tail angles,  $\omega_1$  and  $\omega_2$  with the vector used for the calculation of order parameters and  $g_2(r)$  in pink, for a generic TBD-LC.

Force field parameters for specific molecules or moieties, can be obtained from experimental data, look-up tables and *ab initio* calculations,<sup>56</sup> but obviously it is infeasible to obtain a unique force field for each and every one individually. Therefore, standard force fields, e.g. GAFF (Generalised Amber Force Fields), that have the ability to generate force fields for any arbitrary molecule were developed. The quality of a force field relies on two quantities: the quantitative expression for the energy, and parameter accuracy.<sup>53</sup> For common structures there is a vast array of experimental data for simple moieties, which leads to increased reliability (comparable to that of experiment). With more esoteric groups however, where less data is available, parametrisation can become unreliable. The assumption in force field generation is that standard molecular fragments with known properties will be in the same chemical environment in larger molecules and therefore have the same properties. This is not necessarily true. The MM3 force field for example, that is designed for conjugated carbon frameworks cannot properly describe systems with multiple heteroatoms within the conjugation, since it does not take into account the different environment the heteroatoms produce.<sup>57</sup> GAFF similarly cannot accurately produce force fields for conjugated systems. Optimisations have been made to improve the accuracy for GAFF for certain conjugated aromatics, though.

Dihedrals were corrected by using one of these improved GAFF force fields (GAFF-LCFF, liquid crystal force field)<sup>58</sup> and are of particular importance for the saddle-splay arrangement seen in liquid crystal molecules in HLNCs due to their placement in the core. GAFF-LCFF aims to more accurately represent the expected dihedral distribution of the core-angle of the bent-core mesogens.

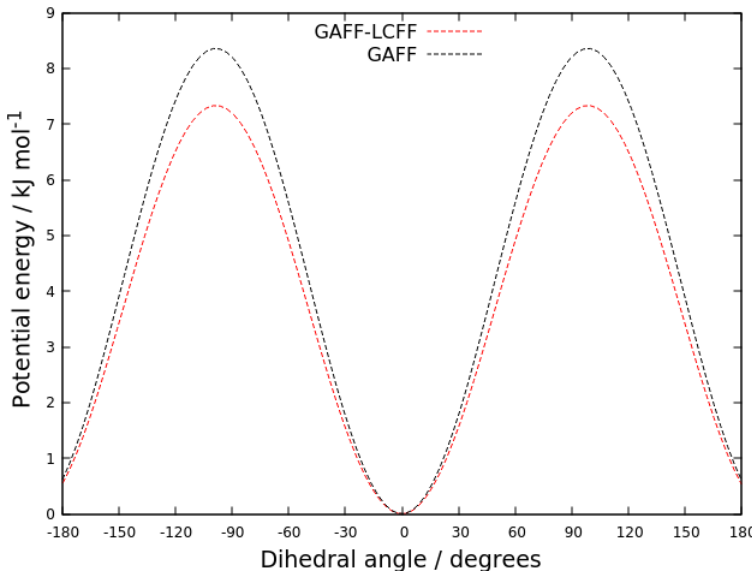


Figure 18: Potentials for the dihedrals of the phenyl benzoate fragment in the TBD-LCs using the Ryckaert-Bellemans coefficients from both GAFF and GAFF-LCFF.

This was achieved by identifying particular core ester groups and modifying their Ryckaert-Bellemans coefficients (the values of which were altered to be  $\approx 10\%$  lower than standard GAFF) since standard GAFF is known to produce alkyl chains which are too stiff, Lenard-Jones interactions that are slightly too attractive and inflexible ester groups.<sup>59</sup> In practice this meant locating the dihedrals in each molecules topology file and replacing them with the correct GAFF-LCFF coefficients for each moiety.

The GAFF-LCFF improves the accuracy of the core angle distribution (Figure 18.), centering it at the expected value of roughly 120 degrees,<sup>60</sup> compared to the larger value of the un-optimised force field. There are a small number of conformations with a core angle of around 50 degrees, this is due to the modified Ryckaert-Bellemans coefficients of GAFF-LCFF being smaller, allowing easier sampling over the barrier needed for the molecule to twist out of plane, and allowing it to collapse.

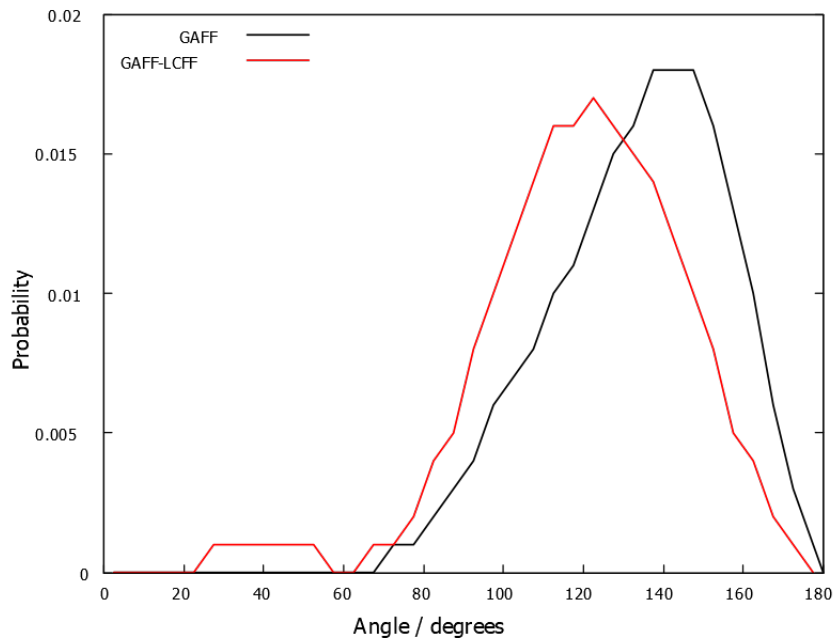


Figure 19: Core-angle distribution of both GAFF and GAFF-LCFF for m,p-TBD. GAFF-LCFF produces an core-angle distribution with a mean closer to the expected value.<sup>15</sup>

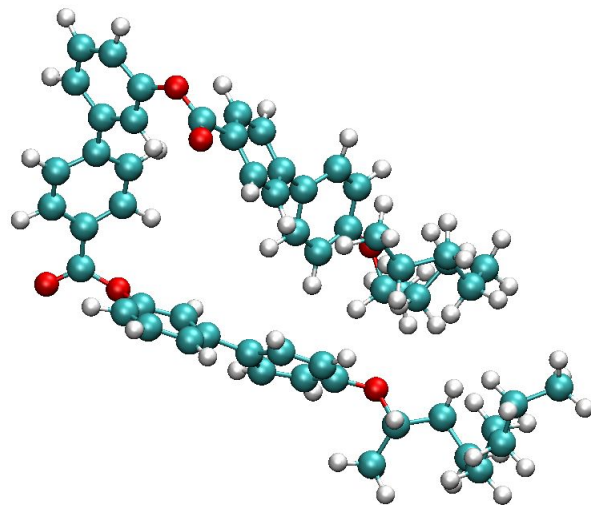


Figure 20: An example of a collapsed molecule due to out of plane twisting.

### 3.1.2 Stochastic Dynamics Gas Phase Simulations

Stochastic Dynamics simulations of single molecules were run in order to understand the distribution of conformations of a single molecule, to be compared to bulk simulations and to verify the modified GAFF force field. Simulations were performed between 350 – 375K for 500,000,000 steps with a timestep of 2 fs, with coordinates

outputted every 5000 frames, creating 500,000 snapshots. This corresponds to a total run time of 1  $\mu$ s with a snapshot every 200 ps, at each temperature. The average core-angle (Figure 17.) was calculated using the GROMACS ‘gangle’ utility, and is defined as the angle between two vectors, one vector parallel to each side of the core.

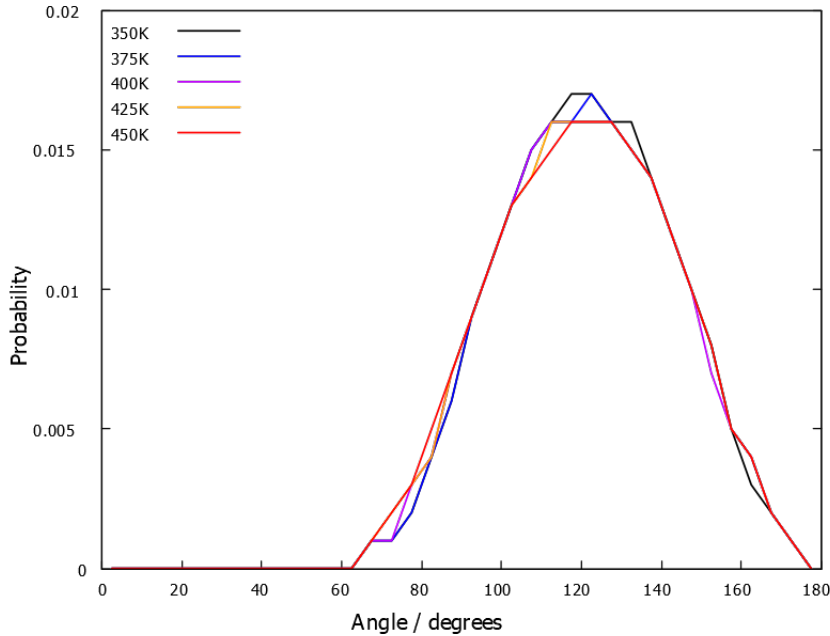


Figure 21: Core-angle distributions over the temperature range 350 – 450K for m,p-TBD using GAFF-LCFF.

The core-angle is fairly invariant, with its peak value staying at around 120°, with a slight broadening at higher temperatures due to the higher energy conformations becoming accessible.

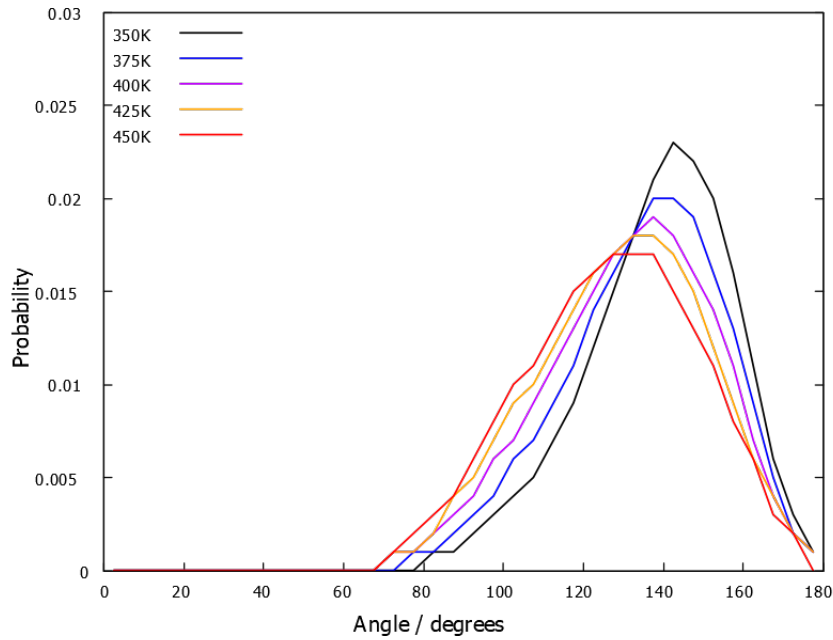


Figure 22: Core-angle distributions over the temperature range 350 – 450K for m-TBD using GAFF-LCFF.

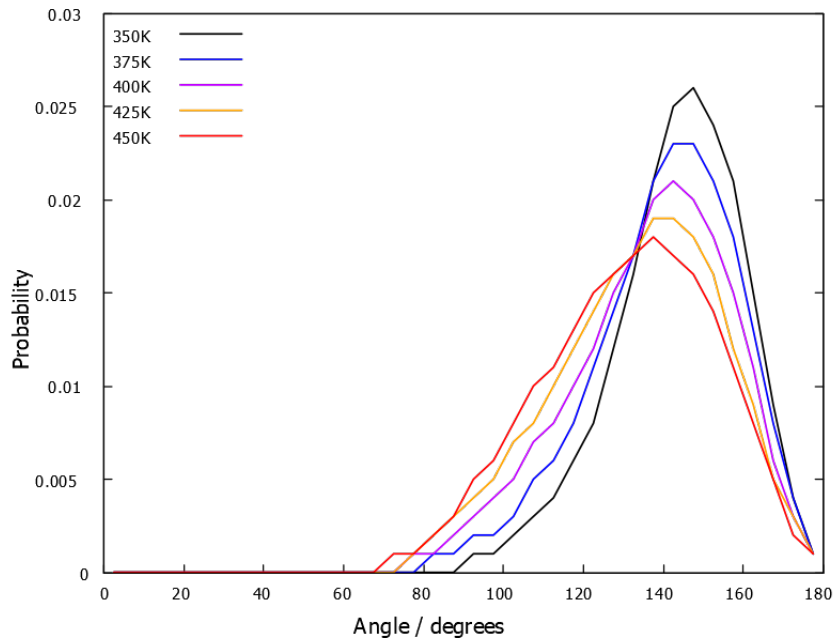


Figure 23: Core-angle distributions over the temperature range 350 – 450K for p-TBD using GAFF-LCFF.

Both m-TBD & p-TBD (Figures 22 and 23) show a more significant change with temperature than m,p-TBD, with the mean angle decreasing by  $\approx 10^\circ$  from  $140^\circ$  to  $130^\circ$ , and a more significant broadening with temperature, due to increased sampling. The decrease in the mean value of the core angle is probably due to

conformations with higher activation energies that are twisted out of plane becoming populated, this new molecular geometry allows collapsing of the core. The reason for both the core angle of m-TBD and p-TBD decreasing as well as flattening but not m,p-TBD is unclear, perhaps the introduction of both methyl groups introduces steric considerations that prevent the core from collapsing.

### 3.2 Atomistic Bulk Phase Simulations

Molecular dynamics simulations of 200 molecules for all three TBD-LCs were performed at various temperatures around the nematic-isotropic transition point. Mesogens were inserted into the box at random orientations, and NVT equilibration was done for 500 ps using the Berendsen thermostat.<sup>61</sup> NPT equilibration was done using the Berendsen barostat/thermostat at 100 bar until empty space was removed and the systems became isotropic. The systems were equilibrated for 50 ns at 1 bar for each temperature, and bond lengths were constrained to their equilibrium lengths with the LINCS algorithmn,<sup>62</sup> with a timestep of 2 fs. Production runs were simulated for a further 72 ns at 1 bar for each temperature similarly, but using the Nose-Hoover thermostat<sup>63</sup> and Parrinello-Rahman barostat.<sup>64</sup> Coordinates were outputted every 5000 frames. Temperatures that showed evidence of a phase transition were ran for upwards of 500 ns. Systems were cooled linearly from 450K in graduations of 25K, this temperature range was chosen based on the isotropic-nematic phase transition temperatures of the mesogens at  $\approx 380\text{K} - 430\text{K}$ .<sup>15</sup>

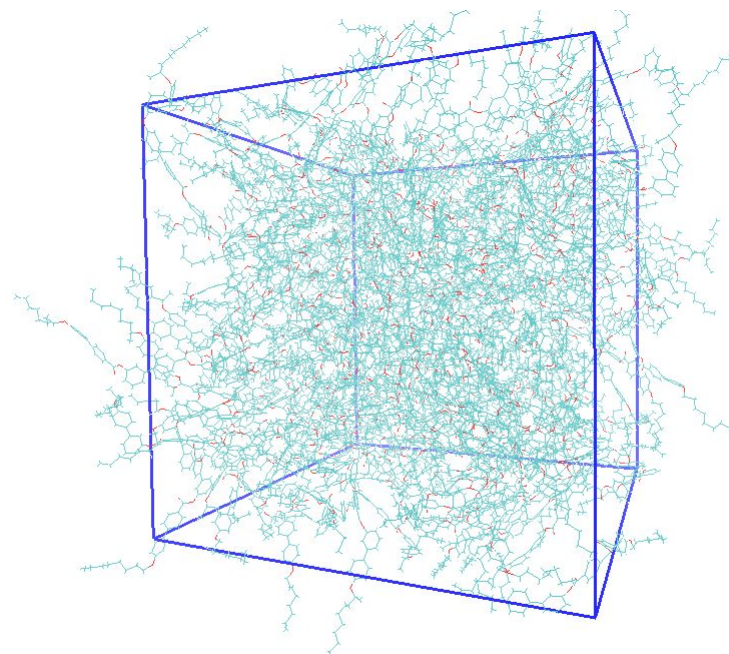


Figure 24: Atomistic simulation of 200 molecules of p-TBD at 375K after approximately 500 ns.

Systems were monitored for equilibration at each temperature through their density. Although density can be used as a proxy for equilibration in most situations, it is important to keep in mind that it is hard to tell if the system really is equilibrated or is in a meta-stable state and transitioning slowly to its true ‘final’ state, especially when the density of say a nematic phase is not much different than the isotropic phase. Therefore, more in-depth analysis is needed to assess whether a phase transition has occurred (or is occurring).

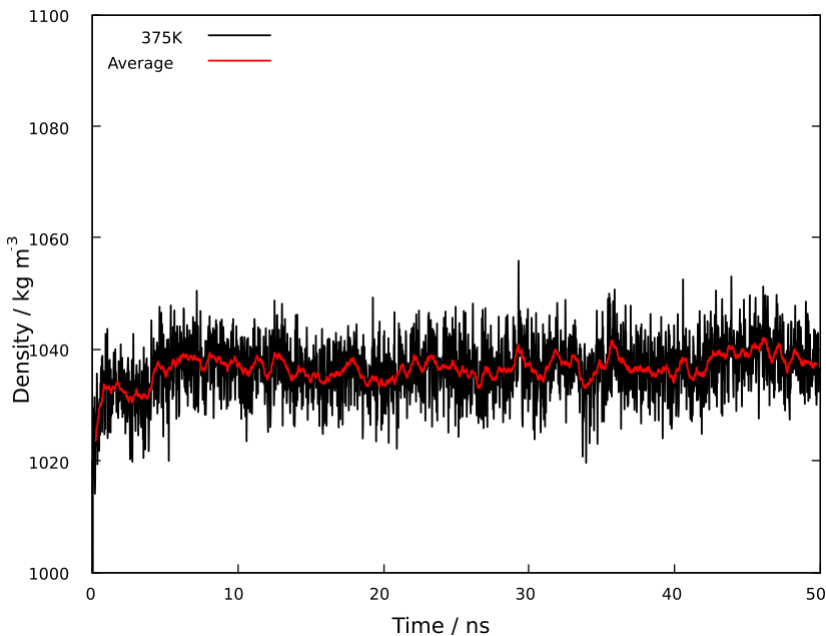


Figure 25: Density for an exemplar equilibration of p-TBD at 375K, with the red line representing a running average of the previous 25 points.

### 3.2.1 Core-Angle Dihedral Distributions

The core-angle dihedral distribution ( $\theta$ , Figure 17) was defined as the angle between two vectors, one parallel to each side of the core. The core-angle could illustrate potential structural changes of the molecule prior to or at a phase transition, and was examined for each molecule 350 – 450K. All dihedral distributions were calculated using a FORTRAN program provided by Gary Yu. All trajectories were obtained from systems that utilise the procedure outlined in section 3.2.

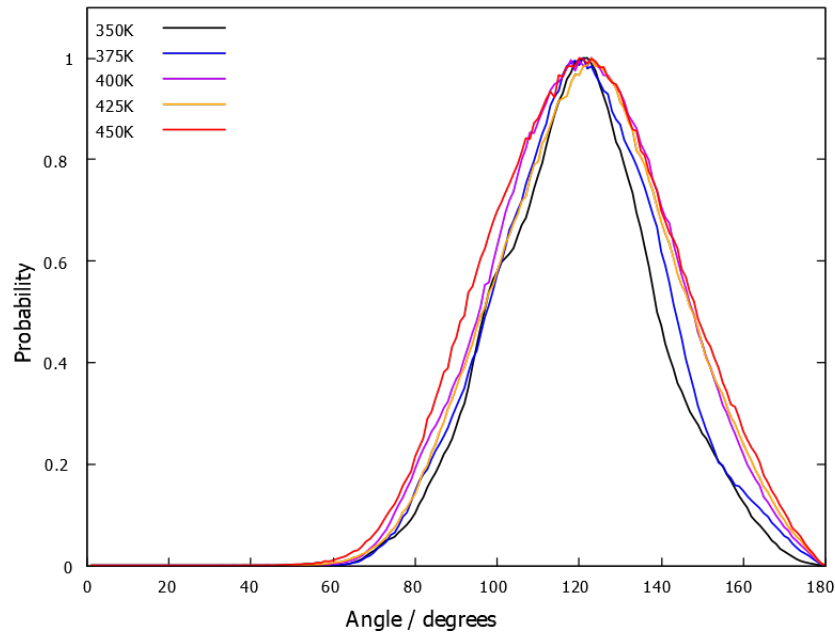


Figure 26: Core-angle distribution, over the temperature range 350 – 450K for m-TBD.

There is a fairly broad distribution of core-angles, indicating flexibility in the core, with a slight narrowing of the distribution at lower temperatures. There is also a slight reduction in the mean core-angle as temperature is lowered.

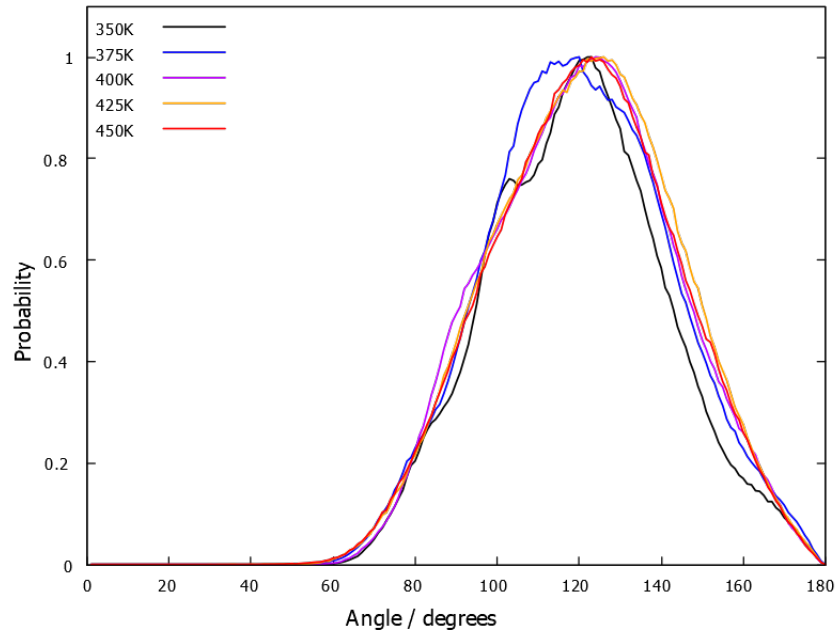


Figure 27: Core-angle distribution, over the temperature range 350 – 450K for p-TBD.

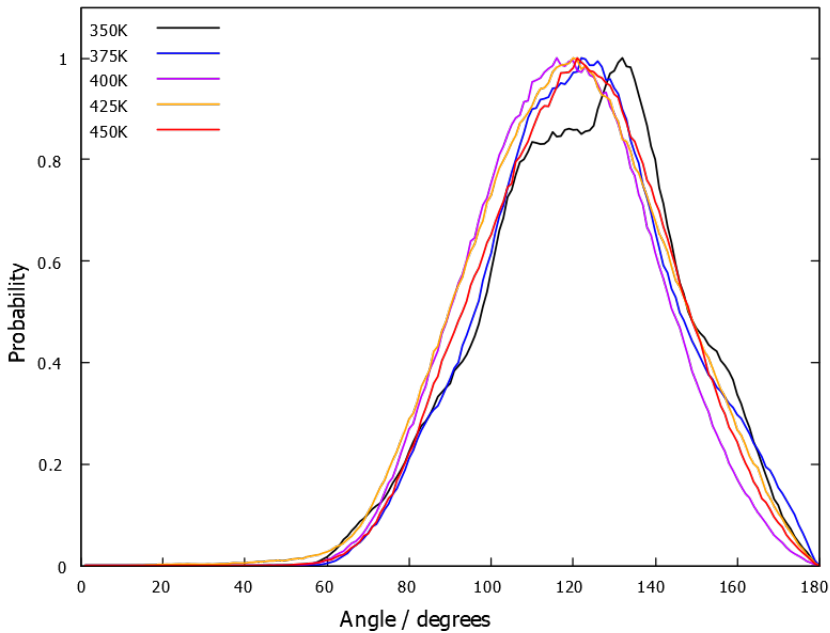


Figure 28: Core-angle distribution, over the temperature range 350 – 450K for m,p-TBD.

The same broad distribution of the core-angles seen in Figure 26 remains for both p-TBD and m,p-TBD. Centered on the same value at higher temperatures the core-angle distribution again narrows with temperature due to the mesogens not being able to access higher energy conformations in the colder systems, as well as colder systems having more close contact with surrounding molecules. This is perhaps indication of pre-transitional structure starting to appear. The sharp peak appearing at 350 K for both p-TBD and m,p-TBD (Figures 27, 28) is probably associated with the appearance of a preferred packing arrangement with the peak occurring at a temperature similar to that of the isotropic-nematic phase transition.<sup>15</sup> The same peak is not seen for m-TBD however, due to the meta side being shorter and so chiral substitution has a smaller effect on that side. For singly chiral centered mesogens, it is clear that chiral substitution on the para side has the most effect on core-angle distribution. Para side substitution has previously been shown to have a larger effect on mesophase formation due to the integral role of the core in the saddle-splay arrangement of mesogens in the B4 phase.<sup>15</sup>

The emergent peak at 350K for p-TBD has a value closer to that of the mean value for the higher temperatures, compared to the emergent peak in the distribution of m,p-TBD. This suggests that although chiral substitution on the meta side in isolation produces no change with temperature, in tandem with substitution on the para side, it produces an effect larger than the sum of its parts. That is to say, meta substitution alone produces nothing, but meta substitution on a mesogen with

a chiral centre on the para side elicits conformational change.

In comparison to the gas phase (Figures 21 – 23), the bulk core angles are  $\approx 20^\circ$  smaller, due to the influence of nearby molecules forcing the core closer together.

### 3.2.2 Meta-Side Core-Tail Dihedral Distributions

The meta side core-tail dihedral distribution ( $\omega_2$ , Figure 17) was defined as the angle between two vectors, one parallel to the meta side of the core, and another parallel to the alkyl chain. The core-tail distribution could illustrate potential structural changes of the molecule prior to or at a phase transition, and was examined for each molecule 350 – 450K. All trajectories were obtained from systems that utilise the procedure outlined in section 3.2.

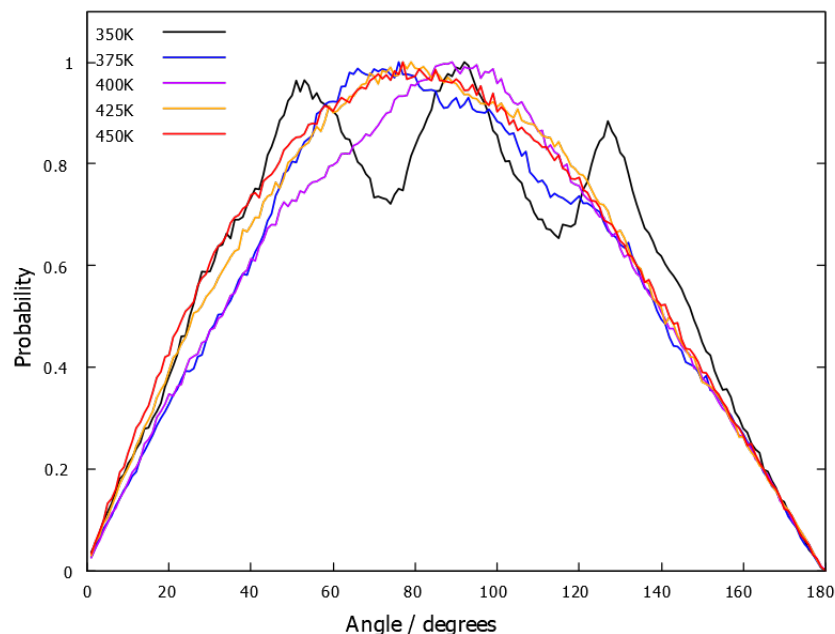


Figure 29: Core-tail distribution for the meta side of p-TBD at 350 – 450K.

The mean angle is  $\approx 80^\circ$ , but with the distribution developing two extra symmetric peaks at 350K, appearing at  $50^\circ$  and  $140^\circ$ , this structure appearing is potentially evidence of a phase transition.

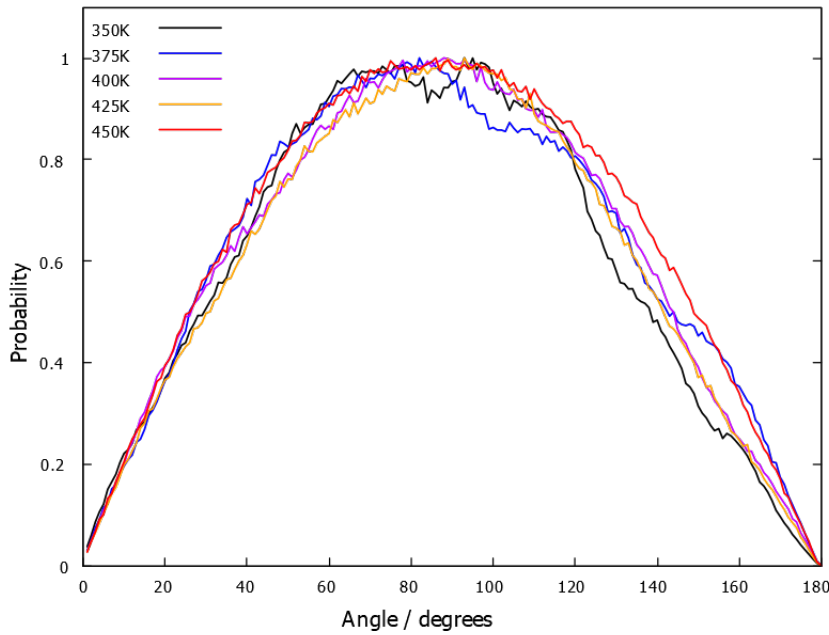


Figure 30: Core-tail distribution for the meta side of m-TBD at 350 – 450K

A broad distribution of the core-tail dihedral is seen with a mean value of  $\approx 80^\circ$ , the same as Figure 29. There is a slight narrowing on cooling due to higher energy conformations becoming less accessible. Interestingly there is little change on cooling, compared to p-TBD. Again showing the lack of significant impact of chiral substitution on the meta side.

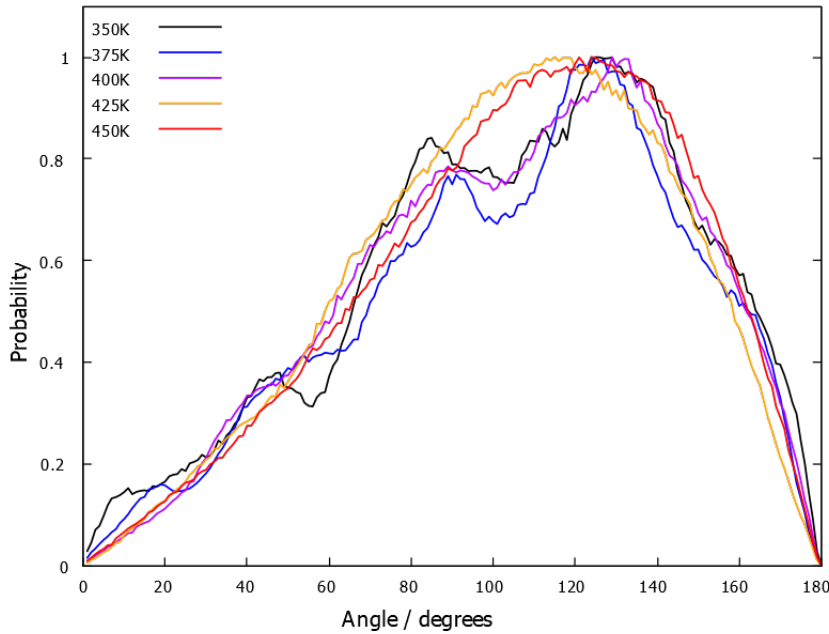


Figure 31: Meta side core-tail distribution for m,p-TBD at 350 – 450K.

The average angle for the core-tail distribution for m,p-TBD is  $\approx 120^\circ$ , much

higher than both m-TBD and p-TBD. The broad distribution becomes bimodal with cooling, a secondary peak appearing at  $\approx 90^\circ$ , and a third peak at  $\approx 40^\circ$  appearing at 350K. A much larger effect is seen on the distribution of the meta side than in Figure 30 since there is double chiral substitution, a similar effect as seen in Figure 28.

The distribution of peaks in p-TBD is symmetric (Figure 29), but m,p-TBD is skewed towards a larger angle. Bent-core nematics are known to have core-tail elongation (more ‘rodlike’) in the nematic phase,<sup>65</sup> and so this bias to larger angles could be evidence of a nematic phase transition.

### 3.2.3 Para Core-Tail Dihedral Distributions

The meta side core-tail dihedral distribution ( $\omega_1$ , Figure 17) was defined as the angle between two vectors, one parallel to the para side of the core, and another parallel to the alkyl chain. The core-tail distribution could illustrate potential structural changes of the molecule prior to or at a phase transition, and was examined for each molecule 350K – 450K. All trajectories were obtained from systems that utilise the procedure outlined in section 3.2.

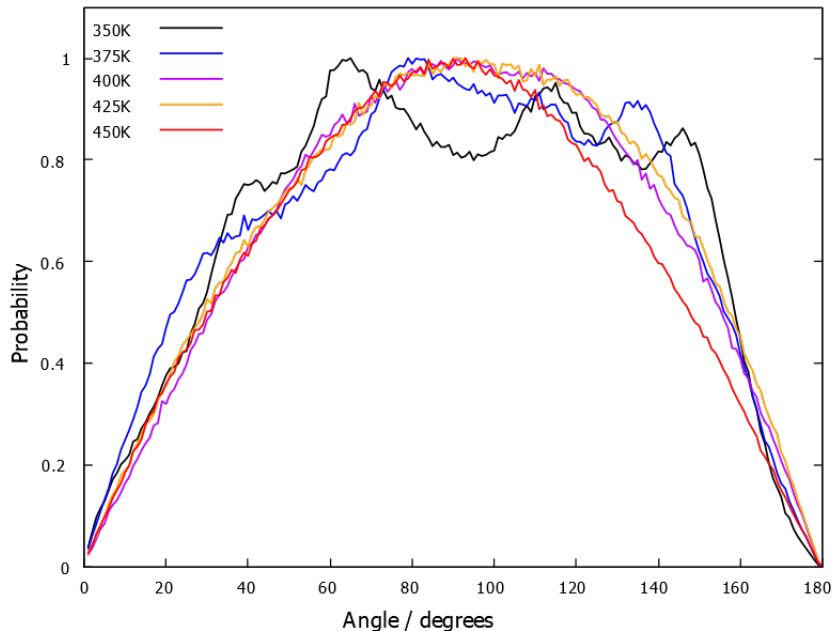


Figure 32: Core-tail distribution for the para side of p-TBD at 350 – 450K.

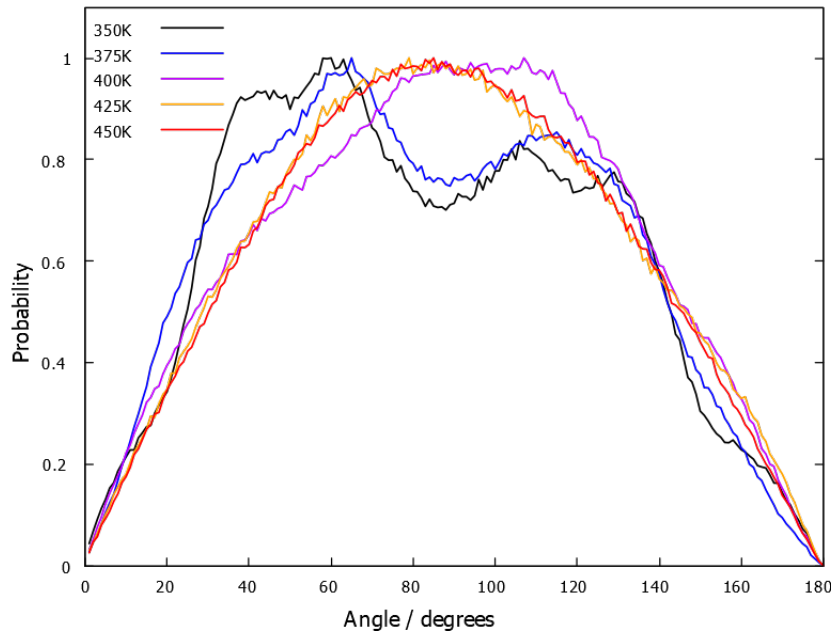


Figure 33: Core-tail distribution for the para side of m-TBD at 350 – 450K.

In both graphs, two peaks appear in the core-tail distribution for the para side of both p-TBD & m-TBD, one peak appearing at  $\approx 40\text{--}60^\circ$  and another at  $120^\circ$ , with a small tertiary peak for p-TBD (Figure 32) at  $\approx 150^\circ$ . This could be some sort of phase transition, due to molecules being closer together and forcing the tail to adopt angles away from conformations where the tail is orthogonal to the core ( $90^\circ$ ) and so a narrower range of conformations are available, resulting in the two peak structure appearing.

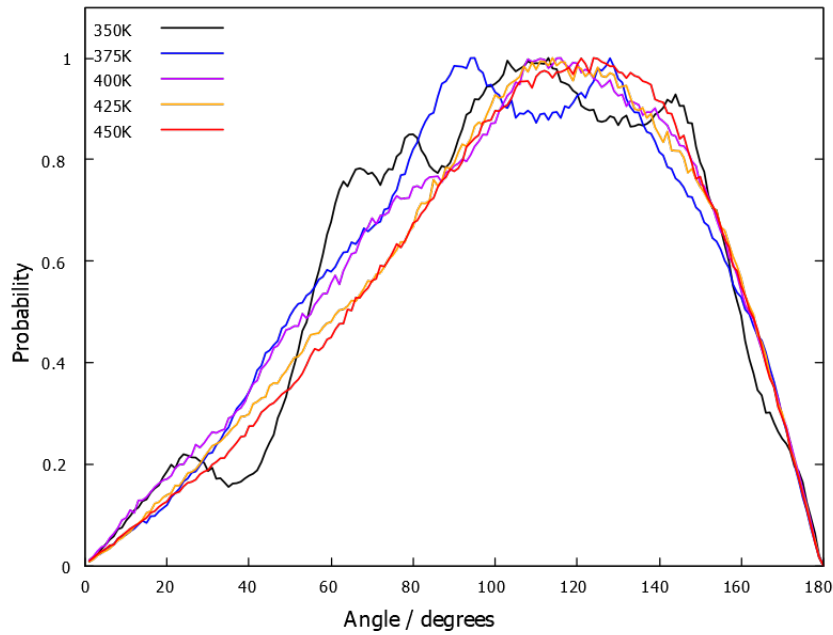


Figure 34: Core-tail distribution for the para side of m,p-TBD at 350 – 450K.

The core-tail distribution for the para side of m,p-TBD is of the same general character as the meta side (Figure 31), with a mean value of  $\approx 120^\circ$  and structure starting to appearing at approximately 375K, with increasingly definite structure at 350K. There is disfavouring of conformations at around  $40^\circ$  at 350K compared to higher temperatures, which is absent on all other core-tail distributions. This disfavouring could represent the bulk becoming more dense, and mesogens coming into closer contact with each others tails and therefore having to either collapse to a smaller angle of  $\approx 20^\circ$  or elongate to  $\approx 60^\circ$ , with elongating to the larger angle preferred. Again, elongation is associated with the nematic phase.

The para side for both m-TBD and p-TBD have the same general shape at lower temperatures, with m-TBD (Figure 33) having a more definite structure.

### 3.2.4 Comparison of Meta and Para Core-tail Distributions.

Adding a chiral centre to the para side of the mesogen is known to have a larger effect on conformational and mesomorphic properties, the mesogen m,p-TBD is ripe for the interrogation of the effect of chiral substitution since both sides have a chiral centre.

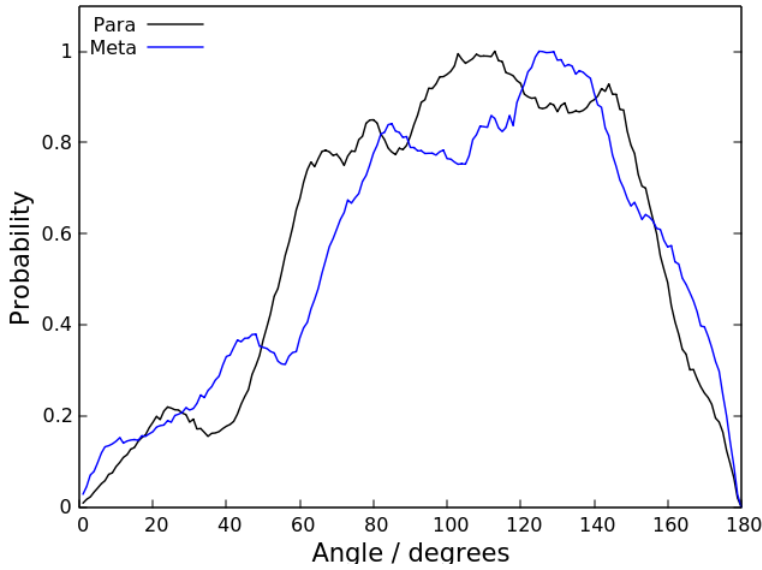


Figure 35: Comparison of the core-tail distributions for the meta and para sides of m,p-TBD at 350K.

The para side has a more significant change in structure relative to the meta side, with a more significant population of smaller core-tail angle conformations as well as a disfavouring of conformations with an angle of  $\approx 40^\circ$ .

### 3.2.5 Density

Density was calculated using the GROMACS 'energy' utility. Density can be used to track the equilibration of the systems, since it is intimately related to temperature, as well as potentially being able to show evidence of phase transitions.

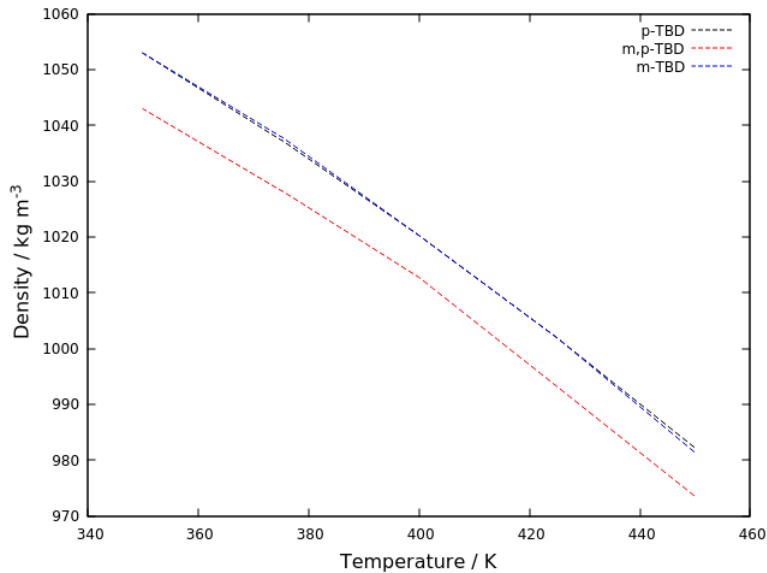


Figure 36: Density of the 3 mesogens from 350 - 450K

Density decreases with temperature linearly, as would be expected, with no evidence of a phase transition. Both m-TBD & p-TBD have the same density, indicating that the introduction of a single chiral centre has no impact on packing. The mesogen m,p-TBD, however, has a lower density which is evidence that double chiral substitution has an effect on bulk structure. The influence due to both chiral groups potentially prevents efficient packing.

### 3.2.6 Mean Squared Displacement

Mean Squared displacement and diffusion coefficient was calculated via the GROMACS 'msd' utility. Diffusion coefficients can be used to assess whether a system has vitrified.

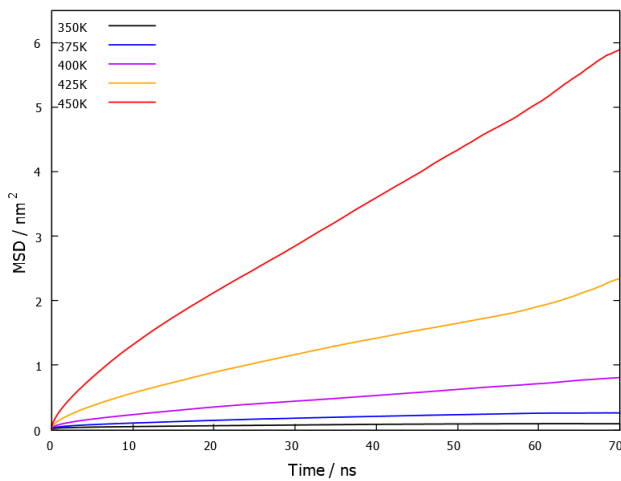


Figure 37: Mean squared displacement for m-TBD from 350 - 450K.

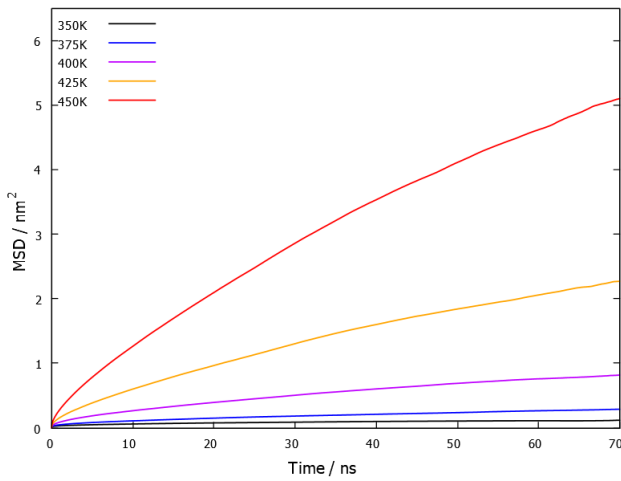


Figure 38: Mean squared displacement for p-TBD from 350 - 450K.

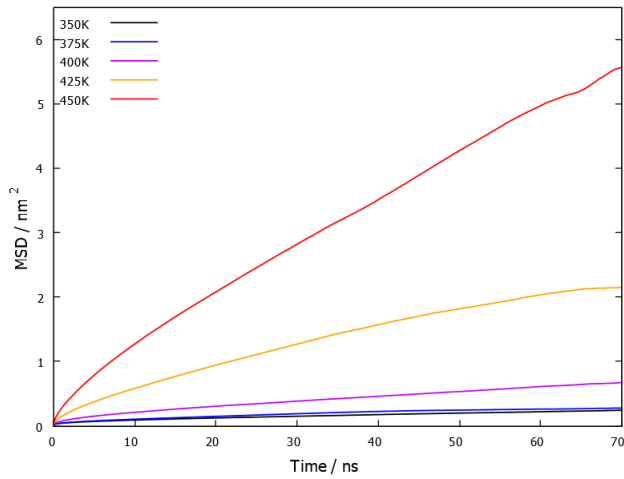


Figure 39: Mean squared displacement for m,p-TBD from 350 - 450K.

The mean squared displacement decreases with temperature, indicating an increase in viscosity. Using mean squared displacement, the viscosity of each system can be determined and diffusion coefficients can be used to elucidate whether any sort of phase change has occurred. The diffusion coefficient is 0 within error at 350K indicating that the system has undergone a phase change. All trajectories were obtained from systems that utilise the procedure outlined in section 3.2.

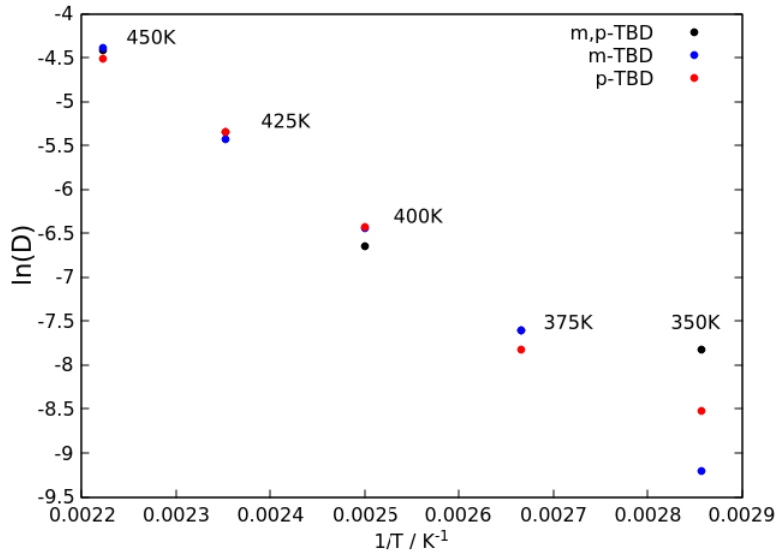


Figure 40: Arrhenius plot for each mesogen from 350 – 450K. A discontinuity is evident between 350K and 375K, indicating a phase change.

The diffusion coefficients decrease with temperature, with the Arrhenius plot for m-TBD decreasing linearly. Both p-TBD and m,p-TBD show evidence of a phase transition between 350K and 375K with a discontinuity (Figure 40), with m,p-TBD showing a more significant change. This is commensurate with the change in both

the core-tail and core-angle distributions, for p-TBD and m,p-TBD in the same temperature range. It is also in the same range as the experimental value for the temperature of the nemataic-isotropic transition. As mentioned previously, para side substitution has a more significant effect owing to its position in the chain (it is further from the core). Although the meta substituted side doesn't introduce any significant effect on its own, in concert with the para side, it affords a greater change in the diffusion coefficient than with just the para side alone. It is not clear yet what sort of phase transition this is however, it could simply be vitrification rather than a liquid crystal phase. More analysis of the structure of the system is needed.

Table 1: Summary for p-TBD.

Temperature / K	Density / kg m <sup>-3</sup>	Diffusion Coefficient
350K	1053	0.0002
375K	1037	0.0004
400K	1020	0.0016
425K	1002	0.0048
450K	982	0.011

Table 2: Summary for m-TBD.

Temperature / K	Density / kg m <sup>-3</sup>	Diffusion Coefficient
350K	1053	0.0001
375K	1038	0.0005
400K	1020	0.0016
425K	1002	0.0044
450K	981	0.0124

Table 3: Summary for m,p-TBD.

Temperature / K	Density / kg m <sup>-3</sup>	Diffusion Coefficient
350K	1043	0.0004
375K	1028	0.0005
400K	1013	0.0013
425K	993	0.0048
450K	973	0.0121

### 3.2.7 Order Parameter

Order parameters can be used to assess the structure of a system. The expected order parameter for an isotropic system would decay to  $N^{-\frac{1}{2}}$  due to a finite number of molecules. The vector in Figure 17 was used to calculate order parameters via a FORTRAN program provided by Gary Yu. All trajectories were obtained from systems that utilise the procedure outlined in section 3.2.

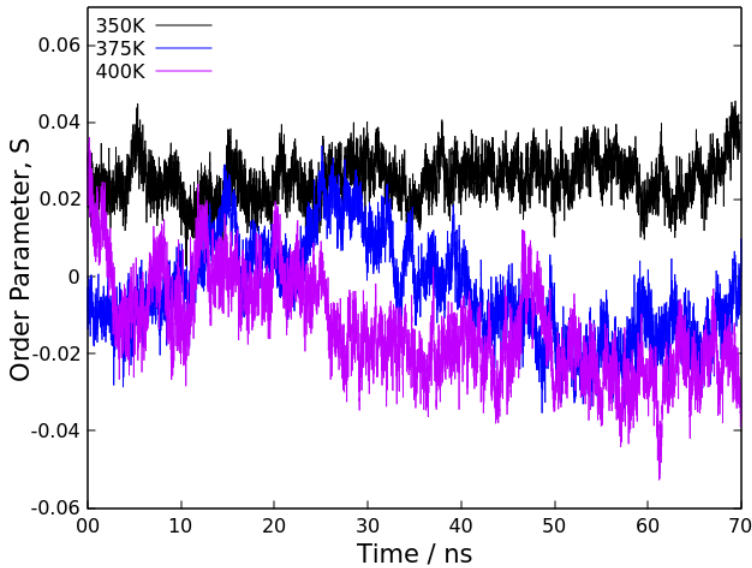


Figure 41: Order parameter for m,p-TBD from 350 – 400K.

Although the order parameter is close to 0 indicating isotropy, and even go slightly negative (a negative order parameter represents orthogonal orientation relative to the director). Bent-core liquid crystals are known to form mesophases in clusters which, depending on the size of the domains, could hard to detect quantitatively. Furthermore, domains of local order could twist in opposite directions and cancel out any effect on the order parameter. The value of the order parameter does increase slightly at lower temperatures however, indicating a slight increase in order. Higher temperatures omitted for clarity, as they were all close to 0. No evidence of mesomorphic structure was found via order parameter, this is not entirely surprising since chiral domain formation requires a nucleation site that might not occur on the timescale that the simulation was run for, as well as lower temperatures having higher viscosities potentially making it difficult for molecules to diffuse to any nucleation point that does occur. All order parameters for each mesogen at every temperature had similar values close to 0, and so were not included. More investigation is needed to establish whether or not these small, undetectable clusters have indeed formed.

### 3.2.8 $g_2(r)$

$g_2(r)$  values can be used to reveal information about short range order, it is a radial distribution function weighted by the square of the cosine of the angle between molecules, and is an important tool to deduce finer grained detail that more global metrics e.g. order parameter might be insensitive to. The vector in Figure 17 was used to calculate order parameters via a FORTRAN program provided by Gary Yu. All trajectories were obtained from systems that utilise the procedure outlined in section 3.2.

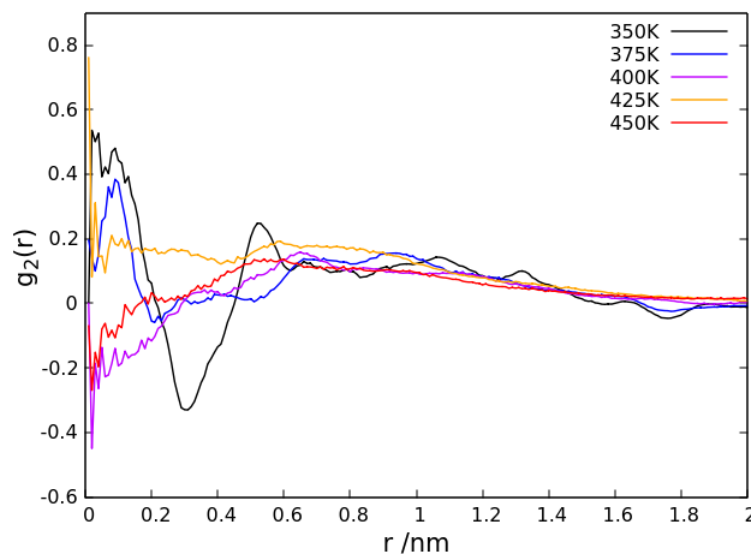


Figure 42:  $g_2(r)$  of m-TBD at 350 – 450K.

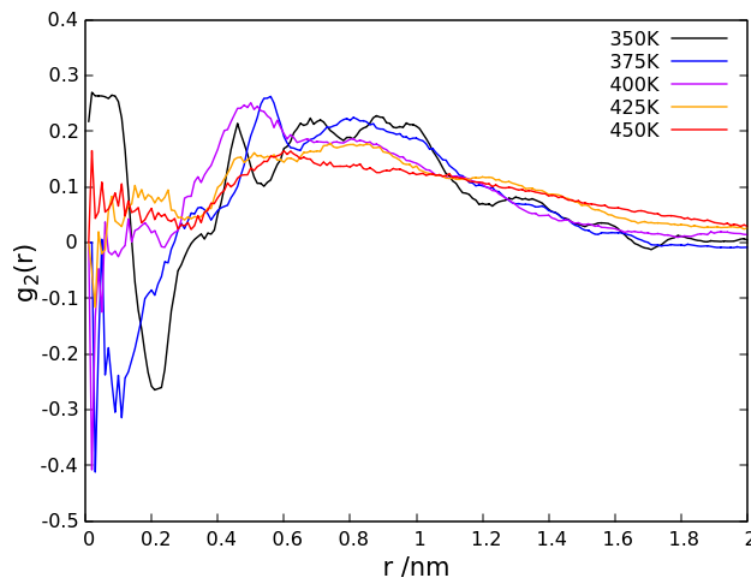


Figure 43:  $g_2(r)$  of p-TBD at 350 – 450K.

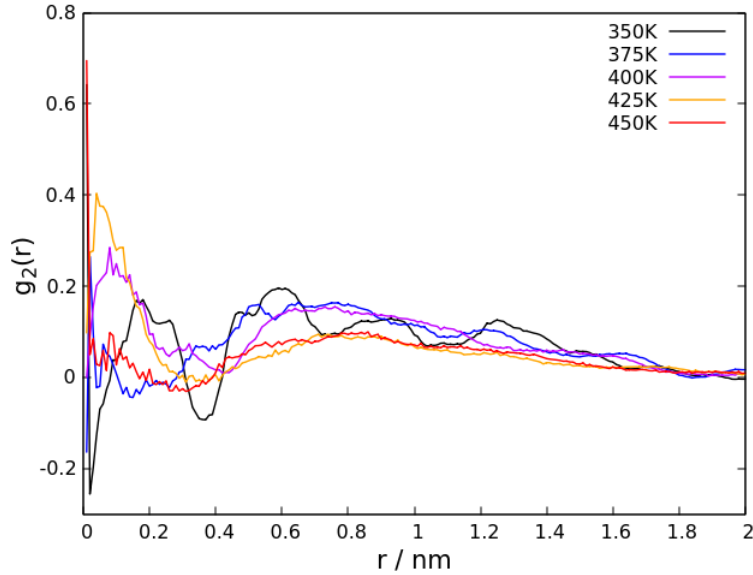


Figure 44:  $g_2(r)$  of m,p-TBD at 350 – 450K.

There is a general trend of an increasing order with cooling, with a peak emerging at 0.8 nm in each system, and with a peak  $g_2(r)$  value of 0.2 – 0.3, a higher positive value indicating more parallel alignment of the vector (shown in Figure 17) representing the core, between mesogens. This is evidence of some short ranged structure starting to appear. A negative  $g_2(r)$  values indicate that mesogens are antiparallel, and this is seen at very short ranges. The value of  $g_2(r)$  tends to 0 at long range, indicating that the bulk is still isotropic, so this is just a short range phenomenon with no overall order.

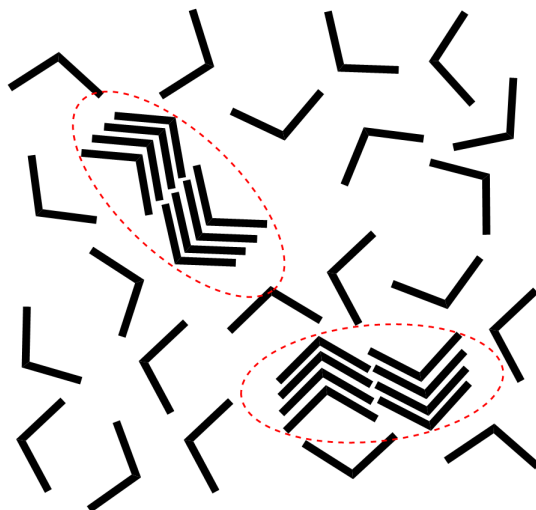


Figure 45: Schematic representation of cybotactic clusters (highlighted) in the isotropic phase.

Bent-core nematics have been shown to form short range clusters on the order of

a few nm, these so called cybotactic clusters can even exist above the clearing point, in the isotropic phase and could be what is represented by the peaks in Figures 42 – 44.<sup>66</sup> These clusters would still mean that there is no global order in the system, and this explanation is consistent with the approximately zero order parameters seen in section 3.2.7.

### 3.3 Coarse-Grained Simulations

An 18 bead coarse-grained model was built using Iterative Boltzmann Inversion as described in section 2.6. Beads were placed at the centre of mass of chosen heavy atoms. Three bead types were used, alkyl, mid and centre, to capture the distinct portions of the mesogens. An XML file was assiduously built, which manually defined the bonded interactions for the coarse-grained model. This was done for each of its 17 bonds, 18 angles and 17 dihedrals. Potentials for these bonded interactions were obtained from a reference atomistic simulation.

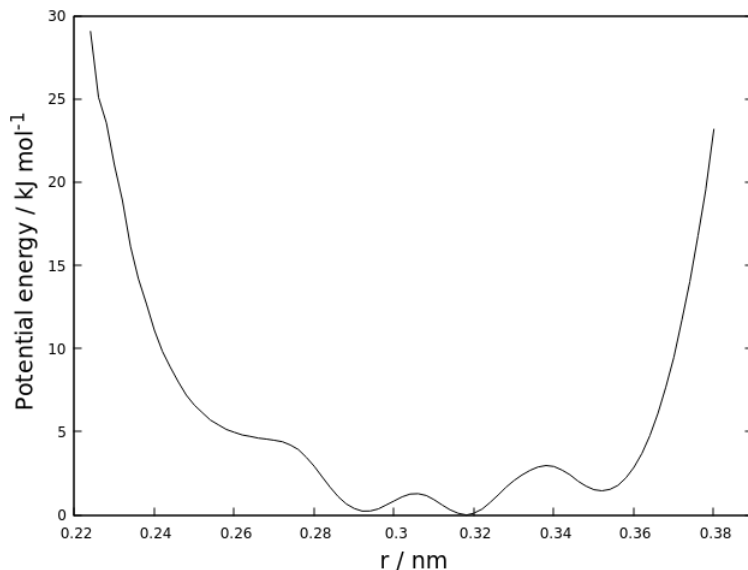


Figure 46: Example of a bonded potential between two alkyl beads.

An atomistic reference of m,p-TBD at 375K was chosen, firstly because of the largest discontinuity in the Arrhenius plot (Figure 40), indicating a significant phase change, and secondly due to m,p-TBD having two chiral centres, which would give the best chance of chiral domain formation. The trajectory was obtained from a system that utilised the procedure outlined in section 3.2.

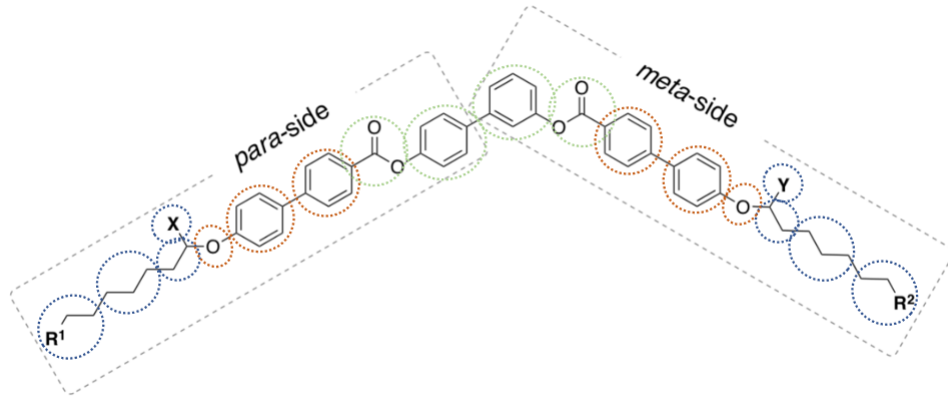


Figure 47: Mapping scheme used for the coarse-grained model. (Alkyl - blue, Mid - orange, Centre - green)

All initial guess non-bonded potentials (Section 2.2.3) for these bonded interactions required individual and manual post-processing. Firstly, by clipping out poorly sampled regions (regions at the extremity that were not smooth), then resampling, which flags the region to be extrapolated. Finally the potentials were extrapolated, which extends the guess potential over the flagged range (1.5 nm). These potentials were then used in GROMACS by editing the topology file for the model, setting all bonded interactions to use these tabulated potentials.

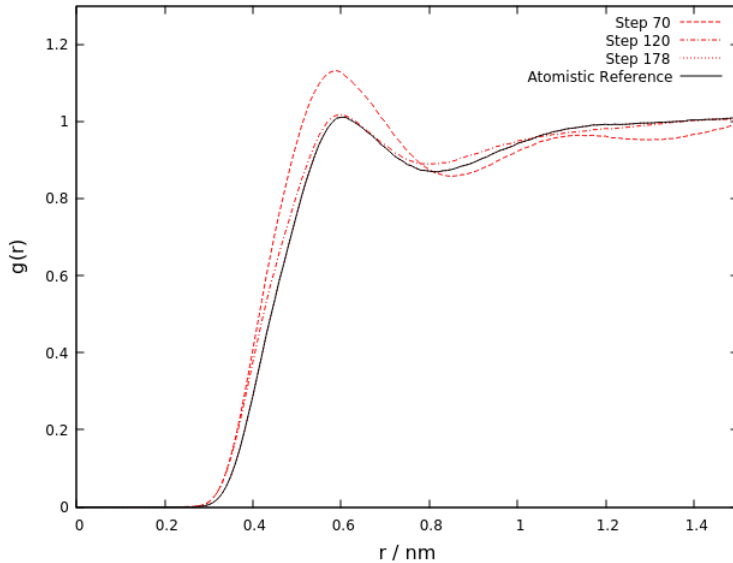


Figure 48: Convergence of the mid-centre non-bonded potential as a function of step number.

Convergence can be aided by adjusting the scale factor for updates as well as omitting iterating over potentials that are already well fitted and could be used in a toy-model. The non-bonded parameters did not converge within tolerance due to

time constraints of the project, but were fairly accurate and taken to do preliminary simulations.

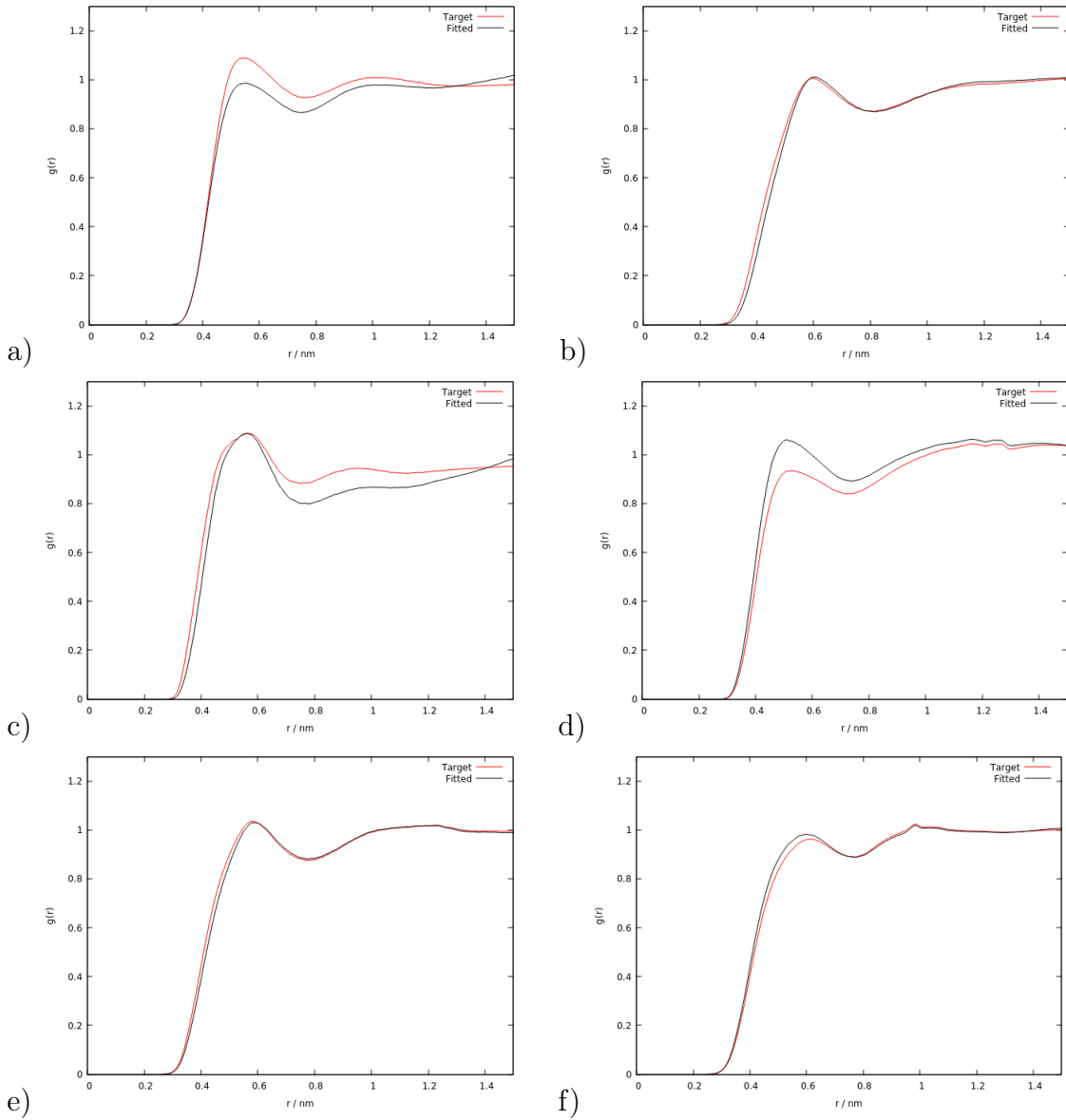


Figure 49: RDFs for non-bonded interactions of m,p-TBD at 375K. a) Alkyl-Alkyl, b) Mid-Mid, c) Centre-Centre, d) Alkyl-Centre, e) Mid-Centre, f) Alkyl-Mid

Although no quantitative results were gained from the coarse-grained model, reasonable non-bonded potentials were fitted. An initial simulations was run with 1600 molecules using the coarse-grained model. It was run for 100 ns initially and behaved like the atomistic simulations.

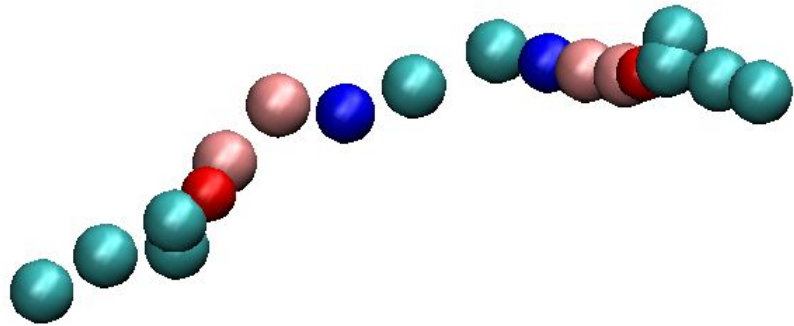


Figure 50: Coarse-grained model for m,p-TBD.

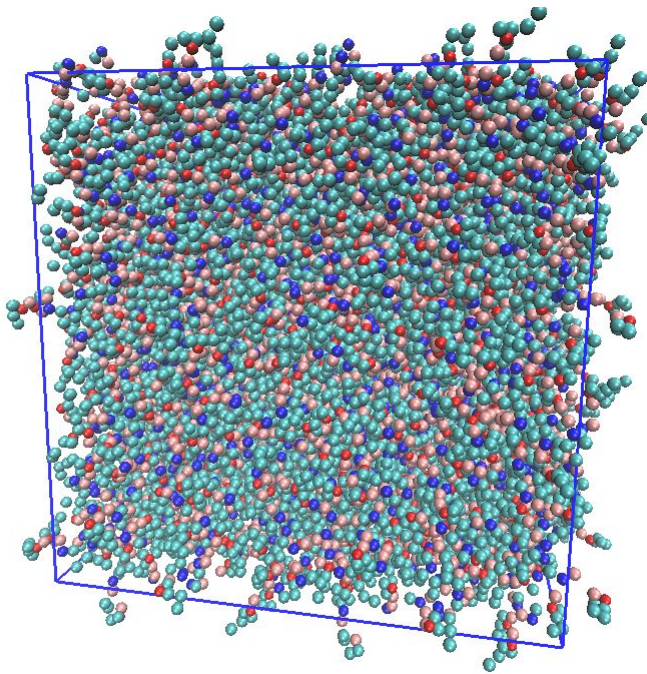


Figure 51: Preliminary coarse-grained system of 1600 molecules of the coarse-grained m,p-TBD. This sort of system could be used to investigate longer timescales than atomistic simulations.

## 4 Conclusion

This project set out to answer two main questions. Firstly, will a phase transition occur in these systems? And secondly, what sort of phase transition will it be?

#### 4.0.1 Atomistic Simulations

To answer these questions, conformational data was obtained for both the gas phase and in the bulk, for three mesogens. The effects of both chiral substitution and temperature on local packing arrangements, as well as molecular geometry of the core and tail of the mesogens was elucidated. Changes in dihedral distributions were observed, with a relatively minor change in molecular structure (a single methyl group). Density as a function of temperature was also investigated, and a slight disparity was observed between m,p-TBD and m-TBD/p-TBD, indicating that the addition of both chiral centres indeed has an effect on the ability of the mesogens to pack closely but adding just one chiral centre to either side causes no appreciable difference, as was observed with m-TBD/p-TBD (Figure 36). Density offered no indication of a phase transition and simply decreased linearly with temperature. Diffusion coefficients and dihedral distributions however, both tentatively showed evidence of a phase transition consonant with the temperature of the experimental value for the isotropic-nematic transition. It is important to establish what sort of transition this is, and whether it is a transition to a liquid crystal phase or just the system becoming too viscous for diffusion/vitrifying, and therefore changing the dihedral distributions of the core and tail, as a result of this increased viscosity.

Order parameters are one way to elucidate what sort of phase transition has occurred, but unfortunately they were not as illuminating as one would hope, consistently averaging values of 0 for all mesogens, at all temperatures studied. This is not too surprising however. The particular mesophases that are expected to form are extremely sensitive to temperature and exist in the range of only a few Kelvin. Simulations were run with rather large temperature gradations of 25K, so the chance of observing any elusive phases on a large scale was slim. This is not the only reason as to why no overall order might have not been observed though. Firstly, although the left-handed stereoisomers were chosen, perhaps this in and of itself is not sufficient to promote one handedness over the other for the chiral domains in this model, leading to the formation of equal and opposite handedness in the domains, if such domains exist at all. Secondly, domains might have only occurred at a small scale around a nucleation point and so are not represented in the value of the order parameter for the entire system.

The qualities of the phase transition, then, can be assessed using two pieces of evidence. Dihedral distributions for the core-tail and core-angle of the mesogens, and  $g_2(r)$  values. Dihedral distributions gave evidence of the emergence of structure at lower temperatures, and of particular interest was the elongation of the core-tail distribution, which is associated with the formation of nematic phases. The evidence for the small scale order, or clusters, (hypothesised as a way for a system

to possess structure but yet have a order parameter close to 0) was obtained via  $g_2(r)$  values. The  $g_2(r)$  values (Figures 42 – 44), showed a slight increase of parallel alignment of the cores of the mesogens at sub nm scale. For these nucleation points of cybotactic clusters to grow larger, it require molecules in the isotropic phase to be able to diffuse towards the site quickly enough to promote growth.<sup>31</sup> With diffusion coefficients close to 0, and molecules unable to diffuse at the temperature where they form (below 375K), it then is not surprising that these domains would be small, hard to detect and not grow even when simulated over longer timescales (500+ ns, as was attempted).

In summary, there is reasonable evidence that some form of a phase transition has occurred, this transition being an amorphous vitrifying of the systems studied, with some preference for parallel alignment in certain domains of the system on a sub nm scale, forming nascent cybotactic structures. These clusters forming in isotropic phases are a well established phenomenon in bent-core mesogens.<sup>67, 68, 69</sup>

#### 4.0.2 Coarse-grained Simulations

The coarse-grained model was refined for as long as possible using IBI techniques, with occasional tuning via scaling parameters for each step and which interactions were being iterated over (say, if one was near perfect it could be left out of the next step to aid convergence of a remaining interactions). Although no quantitative data was obtained, a reasonable toy model resulted which can overcome the main challenge of atomistic simulations - small number of molecules and nanosecond timescales.

### 4.1 Future Work

More work could be done to validate GAFF-LCFF for these particular mesogens, as it was more or less automatically generated, and only preliminary work was carried out to show that GAFF-LCFF was accurate. More extensive techniques could be used, such as Density Functional Theory to generate torsional barrier values. These are especially important, as mesomorphic structures are extremely sensitive, as mentioned previously. Another obvious point of improvement is running simulations for far longer to see if any mesophases emerge with most systems only being run for 70 ns, and particular promising temperatures ran for at most a few hundred ns. Formation of mesophases is to some degree random and might only occur on far larger timescales than is feasible, for example, the bulk could exist in a meta-stable state and for a phase transition to occur, would require a nucleation point, which could require very fortuitous circumstances (and could occur only at temperatures

where diffusion is slow). Again, system can seem thermodynamically equilibrated but in reality be progressing to its final state.<sup>70</sup> A smaller resolution for temperature changes could also be of interest, since mesophases are so sensitive to temperature, as well as allow the choosing of a temperature which permits a nematic phase transition. A temperature that has a (non zero) viscosity that allows growth of any chiral/nematic domains that do indeed form. If a temperature is chosen that causes the system to vitrify, cybotactic clusters might not grow irrespective of the length of the simulation, because nothing is moving. The size and shape of the box is also an important factor that was neglected in this project, with correct length appropriate for the expected helical pitch perhaps promoting more interesting structures. Repulsive potentials could also be added to the ends of the box to anchor mesogens, and help domains grow. Visual inspection is also another potential method of discerning structure, although it was not very useful in this context due to the systems generally being isotropic, tools could be deployed to allow visual analysis more practical, such as colouring molecules by their relative orientation to show nascent chiral domains forming.

A lack of proper nucleation points, and their growth seemed to be the main obstacle to overcome. This wasn't helped by the fact a homogenous system was used, which could also pose some challenges for the creation of liquid crystal phases. Chiral 'dopants' could be added to induce nucleation by reducing the energy barrier required for them to be formed (Figure 9.).<sup>71,72</sup> Pressure could also be varied and perhaps facilitate a phase change, with all simulations in this project performed at 1 bar.

An achiral mesogen would have been a useful control variable, to properly assess the impact of chiral substitution on the properties of the mesogens. All mesogens that featured in this project had at least one chiral centre and so it was not possible to discern what properties the achiral side had inherently, and what was due to merely moving the chiral centre to the other side. The causality of some of the data is also not clear, for example was it a phase change that caused different core-tail distributions, or was it the core-tail distributions that caused the phase change? More investigation is needed.

The coarse-grained model can be refined further in order to correctly reproduce the reference atomistic model, and could eventually be used to provide quantitative data. Perhaps other forms of coarse-graining could be explored, e.g. Dissipative Particle Dynamics (DPD). This technique uses point particles interacting with 'soft' potentials which allows time and length scales that are similar to experimental ones.<sup>73</sup> The increased length scales potentially afforded by this model would allow

more to be learned about these bent-core mesogens.

All of this sort of work is in order to understand the novel properties of bent-core liquid crystals, and for example, allow the generation of mesogens with specific properties. Mesomorphic materials could be the future, and even be used in the creation of molecular machines. These properties are important to understand because their applications could be limitless. As Feynman said, "there is plenty of room at the bottom!".

## References

- [1] R. Cotterill, *The Material World*, Cambridge University Press, 2008.
- [2] H. Kelker, *Molecular Crystals and Liquid Crystals*, 1973, **21**, 1–48.
- [3] T. J. White and D. J. Broer, *Nat. Mater.*, 2015, **14**, 1087–1098.
- [4] D. J. Gardiner, S. M. Morris and H. J. Coles, *Sol. Energy Mater. Sol. Cells*, 2009, **93**, 301–306.
- [5] I. Grabchev, I. Moneva, V. Bojinov and S. Guittonneau, *J. Mater. Chem.*, 2000, **10**, 1291–1296.
- [6] B. R. Kaafarani, *Chemistry of Materials*, 2011, **23**, 378–396.
- [7] D. Andrienko, *Journal of Molecular Liquids*, 2018, **267**, 520–541.
- [8] R. J. Witonsky and J. W. Scarantino, *Liquid crystal thermometer*, 2001, US Patent 6,257,759.
- [9] M. Mitov and N. Dessaud\*\*, *Liquid Crystals*, 2007, **34**, 183–193.
- [10] P. Keating, *Molecular Crystals*, 1969, **8**, 315–326.
- [11] P. Oswald and P. Pieranski, *Nematic and cholesteric liquid crystals: concepts and physical properties illustrated by experiments*, CRC press, 2005.
- [12] D. S. Kim and D. K. Yoon, *Journal of Information Display*, 2018, **19**, 7–23.
- [13] R. Meister, M.-A. Hallé, H. Dumoulin and P. Pieranski, *Phys. Rev. E*, 1996, **54**, 3771–3782.
- [14] H. Kim, Y. Yi, D. Chen, E. Korblova, D. M. Walba, N. A. Clark and D. K. Yoon, *Soft Matter*, 2013, **9**, 2793–2797.

- [15] S. Shadpour, A. Nemati, N. J. Boyd, L. Li, M. E. Prévôt, S. L. Wakerlin, J. P. Vanegas, M. Salamończyk, E. Hegmann, C. Zhu *et al.*, *Materials Horizons*, 2019, **6**, 959–968.
- [16] D. Chen, M. R. Tuchband, B. Horanyi, E. Korblova, D. M. Walba, M. A. Glaser, J. E. Maclennan and N. A. Clark, *Nature communications*, 2015, **6**, 1–10.
- [17] M. Bagiński, M. Tupikowska, G. González-Rubio, M. Wójcik and W. Lewandowski, *Advanced Materials*, 2020, **32**, 1904581.
- [18] M. Costello, S. Meiboom and M. Sammon, *Physical Review A*, 1984, **29**, 2957.
- [19] H. Kikuchi, H. Higuchi, Y. Haseba and T. Iwata, SID Symposium Digest of Technical Papers, 2007, pp. 1737–1740.
- [20] J.-D. Lin, S.-Y. Huang, H.-S. Wang, S.-H. Lin, T.-S. Mo, C.-T. Horng, H.-C. Yeh, L.-J. Chen, H.-L. Lin and C.-R. Lee, *Optics express*, 2014, **22**, 29479–29492.
- [21] W. Cao, A. Muñoz, P. Palfy-Muhoray and B. Taheri, *Nat. Mater.*, 2002, **1**, 111–113.
- [22] J. Goodby, V. Görtz, S. Cowling, G. Mackenzie, P. Martin, D. Plusquellec, T. Benvegnu, P. Boullanger, D. Lafont, Y. Queneau *et al.*, *Chemical Society Reviews*, 2007, **36**, 1971–2032.
- [23] M. Porras-Gomez and C. Leal, *Liquid Crystals Reviews*, 2019, **7**, 167–182.
- [24] N. A. Lockwood, J. C. Mohr, L. Ji, C. J. Murphy, S. P. Palecek, J. J. De Pablo and N. L. Abbott, *Advanced Functional Materials*, 2006, **16**, 618–624.
- [25] J. Vallamkondu, E. B. Corgiat, G. Buchaiah, R. Kandimalla and P. H. Reddy, *Cancers*, 2018, **10**, 462.
- [26] H. Takezoe and Y. Takanishi, *Japanese journal of applied physics*, 2006, **45**, 597.
- [27] C. Tschierske, *Liq. Cryst.*, 2018, **45**, 2221–2252.
- [28] R. A. Reddy and C. Tschierske, *Journal of materials chemistry*, 2006, **16**, 907–961.
- [29] M. Busch, A. V. Kityk, W. Piecik, T. Hofmann, D. Wallacher, S. Całus, P. Kula, M. Steinhart, M. Eich and P. Huber, *Nanoscale*, 2017, **9**, 19086–19099.

- [30] M. Nakata, Y. Takanishi, J. Watanabe and H. Takezoe, *Phys. Rev. E*, 2003, **68**, 041710.
- [31] D. Chen, J. E. MacLennan, R. Shao, D. K. Yoon, H. Wang, E. Korblova, D. M. Walba, M. A. Glaser and N. A. Clark, *J. Am. Chem. Soc.*, 2011, **133**, 12656–12663.
- [32] S. Taushanoff, K. Van Le, J. Williams, R. J. Twieg, B. K. Sadashiva, H. Takezoe and A. Jákli, *J. Mater. Chem.*, 2010, **20**, 5893–5898.
- [33] B. Sunil, M. Srinatha, G. Shanker, G. Hegde, M. Alaasar and C. Tschiesske, *Journal of Molecular Liquids*, 2020, **304**, 112719.
- [34] R. D.C., *The Art of Molecular Dynamics Simulation*, Cambridge University Press, 2nd edn, 2004.
- [35] H. C. Andersen, *Journal of Computational Physics*, 2004.
- [36] A. Nakano, M. Bachlechner, R. Kalia, E. Lidorikis, P. Vashishta, G. Voyadjis, T. Campbell, S. Ogata and F. Shimojo, *Computing in Science Engineering*, 2001, **3**, 56–66.
- [37] M. S. Friedrichs, P. Eastman, V. Vaidyanathan, M. Houston, S. Legrand, A. L. Beberg, D. L. Ensign, C. M. Bruns and V. S. Pande, *Journal of computational chemistry*, 2009, **30**, 864–872.
- [38] B. F. E. Curchod and T. J. Martínez, *Chemical Reviews*, 2018, **118**, 3305–3336.
- [39] R. Valero and D. G. Truhlar, *J. Chem. Phys.*, 2012, **137**, 22A539.
- [40] J. C. Tully, *J. Chem. Phys.*, 2012, **137**, 22A301.
- [41] A. Tkatchenko and M. Scheffler, *Phys. Rev. Lett.*, 2009, **102**, 073005.
- [42] J. Horton, A. E. A. Allen, L. S. Dodda and D. J. Cole, *J. Chem. Inf. Model.*, 2019, **59**, 1366–1381.
- [43] C. Avendano, T. Lafitte, A. Galindo, C. S. Adjiman, G. Jackson and E. A. Muller, *The Journal of Physical Chemistry B*, 2011, **115**, 11154–11169.
- [44] T. D. Potter, J. Tasche and M. R. Wilson, *Phys. Chem. Chem. Phys.*, 2019, **21**, 1912–1927.
- [45] A. Chaimovich and M. S. Shell, *The Journal of chemical physics*, 2011, **134**, 094112.

- [46] D. Van Der Spoel, E. Lindahl, B. Hess, G. Groenhof, A. E. Mark and H. J. Berendsen, *Journal of computational chemistry*, 2005, **26**, 1701–1718.
- [47] J. Wang, R. M. Wolf, J. W. Caldwell, P. A. Kollman and D. A. Case, *Journal of computational chemistry*, 2004, **25**, 1157–1174.
- [48] J. Wang, W. Wang, P. A. Kollman and D. A. Case, *J. Am. Chem. Soc*, 2001, **222**, U403.
- [49] A. Jakalian, D. B. Jack and C. I. Bayly, *J. Comput. Chem.*, 2002, **23**, 1623–1641.
- [50] A. W. S. Da Silva and W. F. Vranken, *BMC research notes*, 2012, **5**, 367.
- [51] J.-P. Ryckaert and A. Bellemans, *Faraday Discuss. Chem. Soc.*, 1978, **66**, 95–106.
- [52] G. Chang, W. C. Guida and W. C. Still, *Journal of the American Chemical Society*, 1989, **111**, 4379–4386.
- [53] F. Jensen, *Introduction to computational chemistry*, John wiley & sons, 2017.
- [54] V. Rühle, C. Junghans, A. Lukyanov, K. Kremer and D. Andrienko, *J. Chem. Theory Comput.*, 2009, **5**, 3211–3223.
- [55] Fujitsu Kyushu Systems Limited, Japan, SCIGRESS (2016).
- [56] M. González, *École thématique de la Société Française de la Neutronique*, 2011, **12**, 169–200.
- [57] N. L. Allinger, Y. H. Yuh and J. H. Lii, *Journal of the American Chemical Society*, 1989, **111**, 8551–8566.
- [58] N. J. Boyd and M. R. Wilson, *Phys. Chem. Chem. Phys.*, 2015, **17**, 24851–24865.
- [59] N. J. Boyd and M. R. Wilson, *Phys. Chem. Chem. Phys.*, 2018, **20**, 1485–1496.
- [60] M. Hird, *Liquid Crystals Today*, 2005, **14**, 9–21.
- [61] H. J. C. Berendsen, J. P. M. Postma, W. F. van Gunsteren, A. DiNola and J. R. Haak, *J. Chem. Phys.*, 1984, **81**, 3684–3690.
- [62] B. Hess, H. Bekker, H. J. C. Berendsen and J. G. E. M. Fraaije, *J. Comput. Chem.*, 1997, **18**, 1463–1472.

- [63] D. J. Evans and B. L. Holian, *J. Chem. Phys.*, 1985, **83**, 4069–4074.
- [64] M. Parrinello and A. Rahman, *Phys. Rev. Lett.*, 1980, **45**, 1196–1199.
- [65] C. Amovilli, I. Cacelli, G. Cinacchi, L. De Gaetani, G. Prampolini and A. Tani, *Theor. Chem. Acc.*, 2007, **117**, 885–901.
- [66] C. Bailey, K. Fodor-Csorba, J. T. Gleeson, S. N. Sprunt and A. Jákli, *Soft Matter*, 2009, **5**, 3618–3622.
- [67] D. Wiant, S. Stojadinovic, K. Neupane, S. Sharma, K. Fodor-Csorba, A. Jákli, J. T. Gleeson and S. Sprunt, *Phys. Rev. E*, 2006, **73**, 030703(R).
- [68] O. Francescangeli, F. Vita, C. Ferrero, T. Dingemans and E. T. Samulski, *Soft Matter*, 2011, **7**, 895–901.
- [69] S. H. Hong, R. Verduzco, J. C. Williams, R. J. Twieg, E. DiMasi, R. Pindak, A. Jákli, J. T. Gleeson and S. Sprunt, *Soft Matter*, 2010, **6**, 4819–4827.
- [70] A. J. McDonald and S. Hanna, *J. Chem. Phys.*, 2006, **124**, 164906.
- [71] D. R. Link, G. Natale, R. Shao, J. E. MacLennan, N. A. Clark, E. Körblova and D. M. Walba, *Science*, 1997, **278**, 1924–1927.
- [72] F. Araoka, Y. Takanishi, H. Takezoe, A. Kim, B. Park and J. W. Wu, *J. Opt. Soc. Am. B*, 2003, **20**, 314–320.
- [73] P. Español and P. B. Warren, *J. Chem. Phys.*, 2017, **146**, 150901.

## Seminar Summaries

### Evolution Engines - Professor Chris Hunter

DNA is a duplex consisting of phosphate-deoxyribose backbones joined by nucleotide base pairs, and genetic information is encoded by the ordering of these pairs. Analogues of DNA have been created, specifically via templated polymerization, and have been utilised to evolve oligomers with chemically diverse side chains. These oligomers, although structurally different than DNA, use the same non-covalent interactions in their structure e.g. hydrogen bonding and metal-ligand coordination, and have been demonstrated to read and write sequence information. Information is encoded with a two letter alphabet, a phosphine oxide H-bond acceptor and a trifluorophenol H-bond donor. These acceptors/donors are situated on an amine backbone, which is assembled from two components, a diamine linker unit and a dialdehyde

that contains recognition units. Low molarities and a reasonable degree of flexibility afford the synthesis of the backbone (too flexible and the backbone folds, too rigid and the backbone fails to assemble). These two components (donor/acceptor and the backbone) create a duplex that can encode information and has been shown to increase in stability with length which allows the scaling of the amount of information stored, with the ability to independently optimise all aspects of the duplex (synthesis, backbone and recogniton modules).

### **Fluorescent Colloidal SU-8 Polymer Rods - Professor Roel Dullens**

Colloids can be used as a proxy to study liquid crystal phase behaviour, they are analogous to nematogens which can be easily observed. Conventional optical microscopy is an attractive observation technique due to its convenience, but it can be hard to view deep within a sample. 3D confocal microscopy is a way round this problem, and allows penetration within samples. And as such it is commonly used to see the mesomorphic properties of colloids, the refractive index of the colloidal system must be at parity with the solvent to prevent scattering, as well carefully controlling density mismatch to (by varying solvent composition) to induce a sedimentation-diffusion equilibrium in order to observe the isotropic-nematic interface. Colloids were synthesised by shearing SU-8 polymer droplets using a mixer, sonicating the resulting rod-like particles and finally curing them with UV-light. This induces crosslinking, producing stable colloidal particles. Optical traps using AC electric fields are also employed to study nucleation in the isotropic colloidal phase. These colloidal rods offer a stable, and easily synthesised system that can be finely adjusted and purport to offer a new way to elucidate phase behaviour that is directly applicable to liquid crystal systems.